

Comptonization efficiencies of the variability classes of GRS 1915+105

Partha Sarathi Pal^{1,*}

S. N. Bose National Centre For Basic Sciences, Kolkata.

Sandip K. Chakrabarti¹, Anuj Nandi²

ISRO Satellite Centre, Bangalore

Abstract

The Galactic microquasar GRS 1915+105 exhibits at least seventeen types of variability classes. Intra and inter class transitions are reported to be observed within seconds to hours. Since the observation was not continuous, these classes appeared to be exhibited in a random order. Our goal is to predict a sequence of these classes. In this paper, we compute the ratio of the photon counts obtained from the power-law component and the blackbody component of each class and call this ratio as the ‘Comptonizing efficiency’ (CE) of that class. We sequence the classes in the ascending order of CE and find that this sequence matches with a few class transitions observed by RXTE satellite and IXAE instruments on board IRS-P3. A change in CE corresponds to a change in the optical depth of the Compton cloud. Our result implies that the optical depth of the Compton cloud gradually rises as the variability class becomes harder.

Keywords: Black Holes, Accretion disk, X-rays, Radiation mechanism

*Corresponding author

Email addresses: parthasarathi.pal@gmail.com,
partha.sarathi@boson.bose.res.in (Partha Sarathi Pal), chakraba@bose.res.in
(Sandip K. Chakrabarti), anuj@isac.gov.in (Anuj Nandi)

¹S. N. Bose National Centre For Basic Sciences, Kolkata. JD Block, Salt Lake, Kolkata - 700098, India. Tel: +91-33-2335-5706/7/8 Extn: 374, Fax: +91-33-2335-9176.

²Space Astronomy Group, INSAT Building, ISRO Satellite Centre, Bangalore - 560017, India

1. Introduction

The enigmatic stellar mass black hole binary GRS 1915+105 (Harlaftis et al., 2004) was first discovered in 1992 by the WATCH detectors (Castro-Tirado et al., 1992) as a transient source with a significant variability in X-rays (Castro-Tirado et al., 1994). In the RXTE era, GRS 1915+105 was monitored over thousands of times in X-rays and the data reveal a very unique nature of this compact object, in that, the nature of the light curve was highly unpredictable. The radio observation with VLA suggests apparent superluminal nature of its radio jets. Radio observation constrains that its maximum distance is no more than 13.5 kpc and that the jet axis makes an angle of 70° with the line of sight (Mirabel et al., 1994).

Continuous X-ray observation of GRS 1915+105 reveals that the X-ray intensity of the source changes peculiarly in a variety of timescales ranging from seconds to days (Greiner et al., 1996; Morgan et al., 1997). Small scale variabilities of GRS 1915+105 are identified with local variation of the inner disk (Nandi et al., 2000; Chakrabarti et al., 2000a; Migliari et al., 2003). Several observers have reported that this object exhibited many types of variability classes (Yadav et al., 1999; Rao et al., 2000b; Belloni et al., 2000; Chakrabarti et al., 2000b; Naik et al., 2002a). Depending on the variation of photons in different arbitrary energy bands (hardness ratio) and conventional color-color diagram of GRS 1915+105, the X-ray variability of the source was found to have fifteen (α , β , γ , δ , ϕ , χ_1 , χ_2 , χ_3 , χ_4 , μ , ν , λ , κ , ρ , θ) classes. In a 1999 observation of RXTE, the existence of a new class ω was reported (Klein-Wolt et al., 2002; Naik et al., 2002a). In 2003, one other class, namely, ξ was reported (Hannikainen et al., 2005). In the so-called χ (i.e., χ_1 to χ_4) class, the strong variability as is found in other classes is absent. The classes named χ_1 , χ_3 , β and θ are found to be associated with strong radio jets (Naik et al., 2000; Vadawale et al., 2001, 2003). Ueda et al. (2009) presented the results from simultaneous Chandra HETGS and RXTE observations of GRS 1915+105 in its quasi-stable “soft state” (the so-called State A). The continuum spectra obtained with RXTE in the 3–25 keV band is found to be fitted assuming a thermal Comptonization with an electron temperature of ~ 4 keV and an optical depth of ~ 5 from the seed photons from the standard disk extending down to $(4 - 7) r_g$. Most of the radiation energy appears to be produced in the hot electron cloud which completely covers the inner part of the disk. Neilsen et al. (2011) studied in detail the ρ variability class whose spectral and timing properties were found to be

consistent with the radiation pressure instability. At small scales ($1 - 10$) r_g , they detect a burst of bremsstrahlung emission that appears to occur when a portion of the inner accretion disk evaporates due to radiation pressure. Jet activity, as inferred from the appearance of a short X-ray hard state, seems to be happening at times near minimum luminosity, with a duty cycle of ~ 10 %. [Chakrabarti et al. \(2000b\)](#) suggested that not only in ρ , in all the classes, some outflows should be present when the state is harder ([Neilsen et al., 2009](#)), since only in harder states the Compton cloud, which is also the base of the jet in this model, is significantly hot. [Nayakshin et al. \(2000\)](#) investigated different accretion disk models and viscosity prescriptions and concluded that the X-ray observations clearly require a quasi-stable accretion disk solution at a high accretion rate at which the radiation pressure begins to dominate. This excludes the standard α viscosity prescription. They devise a simplified model of a disk with a corona and a modified viscosity law that has a quasi-stable upper branch. Their model appears to account for several gross observational features of GRS 1915+105, including its overall cyclic behavior on timescales of $\sim 100 - 1000$ s. The inclusion of a jet allowed them to reproduce several additional observed features as well. [Cabanac et al. \(2009\)](#) reported that in response to major changes in the mass accretion rate within the inner accretion flow, the black hole binary transients undergo dramatic evolution in their X-ray timing and spectral behavior during outbursts.

Quasi-Periodic Oscillations (QPOs) are observed in GRS 1915+105 in a wide range of frequencies. QPOs in this source are associated with different types of X-ray variabilities and their timing properties are correlated with spectral features ([Muno et al., 1999](#); [Sobczak et al., 1999](#); [Rodriguez et al., 2002](#); [Vignarca et al., 2003](#); [Dunn et al., 2010](#)). The origin of QPO frequencies between 0.5 to 10 Hz is identified to be due to the oscillation of the Compton cloud, presumably the post-shock region of the low angular momentum (sub-Keplerian) flow ([Chakrabarti et al., 2000a](#); [Rao et al., 2000a](#)). There are several other models of QPOs in the literature. For instance, [Mikles et al. \(2009\)](#) state that the low-frequency quasi-periodic X-ray oscillations observed microquasars are correlated to, but do not originate at, the physical radius of the inner edge of the accretion disk. By analyzing several data sets including θ , β , and α they find that accretion-ejection instability (AEI) model may explain the nature of correlations between the frequency and radius.

While a large number of reports appear in the literature on GRS 1915+105, to our knowledge, there is no work which actually asked the question: are these variability classes arbitrary, or they appear in a given sequence? The

problem lies in the fact that no satellite continuously observed GRS 1915+105. Sporadic observations caught the object in sporadic classes, and thus no specific sequence of the variability classes has been identified. In the present paper, we compute a simple parameter obtainable directly from observations. This parameter, which we term as the Comptonization efficiency or CE, is simply the ratio between the number of photons in the power-law component and number of photons in the black body component. This is not simply ‘a’ generic hardness ratio that is often reported in the literature, since the energy bands of the soft and hard photons in our consideration vary dynamically from class to class as decided by the best χ^2 fit. We find that, when averaged over a full cycle (whenever available) or over a sufficiently long time period (whenever there is no obvious periodicity in the light curve), every class is characterized by more or less a unique CE. When these CEs are placed in an ascending order, a sequence of the classes is generated. It appears that the direct class transitions which have been observed so far, do generally take place between the nearest neighboring classes of this particular sequence that we propose. Of course, if the formation of a class (such as the θ , β and α) requires special physical condition, such as the presence of a strong magnetic field, that class may be skipped and the transition could be to the next nearest neighbor. Since the number of photons in the power-law component depends on the degree of interception by the so-called hot electron cloud or Compton cloud (Sunyaev et al., 1980, 1985), CE thus parameterizes different classes by the average optical depth of the Compton cloud. To accomplish the computation of running value of CE, we separate out the photons γ_{BB} of the black body component and the photons γ_{PL} from the power-law component and take the running ratio CE as a function of time to study how the Compton cloud itself varies in a short time scale. Our finding reveals that the Compton cloud is highly dynamic. We present possible scenarios of what might be happening inside it in different variability classes. In this paper, along with the dynamical evolution of CE, we also compute the spectrum and the power density spectrum (PDS) of each of the classes. A preliminary report is presented in Pal et al. (2008).

The paper is organized as follows: in the next Section, we present a general discussion of the observation, our criteria of selection of data and the analysis technique. In §3, we discuss the procedure of calculation that is adopted to calculate the photon numbers. In §4, the results are presented. In §5, we show that the Comptonizing efficiency may be a key factor to distinguish among various classes. Finally, in §6, we make concluding remarks.

2. Observation & Data Analysis

The RXTE science data is taken from the NASA HEASARC data archive for analysis. We have chosen the data procured in 1996-97 by RXTE as in this period GRS 1915+105 has shown almost all types of variabilities in X-rays. Subsequently, in 1999, another class, namely ω was seen. In the present paper, since we are interested in sequencing these seventeen classes, we will rename them as follows: I= ϕ ; II= δ ; III= γ ; IV= ω ; V= μ ; VI= ν ; VII= λ ; VIII= κ ; IX= ρ ; X= ξ ; XI= β ; XII= α ; XIII= θ ; XIV= χ_2 ; XV= χ_4 ; XVI= χ_1 ; XVII= χ_3 . This renaming was done on purpose, since it will turn out that this is the sequence in which average CE ($\langle CE \rangle$) increases.

During the data analysis we exclude the data collected for elevation angles less than 10° , for offset greater than 0.02° and those acquired during the South Atlantic Anomaly (SAA) passage. In Table 1, the details of the data selection and ObsIDs are given which we analyzed in this paper. In the first column, we give the observational ID, in the second column, we present the class number (new and old), and finally, in the third column, we present the date of observation.

Here we discuss how we analyzed the temporal and spectral properties of the data.

2.1. Timing Analysis

In the timing analysis of the RXTE/PCA data we use “binned mode” data which was available for 0-35 channels only, with a time resolution of 2^{-7} sec. We use the ‘event mode’ data with a time resolution of 2^{-8} sec for the rest of the channels. We restrict ourselves in the energy range of $\sim 2 - 40$ keV for the timing analysis of PCA data. After extracting the light curves using standard tasks from two different modes, we add them by the FTOOLS task “lcmath” to have the whole energy range light curve (2 to 40 keV). The Power Density Spectrum (PDS) is generated by the standard FTOOLS task “powspec” with a suitable normalization. The data is re-binned to 0.01s time resolution to obtain a Nyquist frequency of 50 Hz as the power beyond this is found to be insignificant. PDSs are normalized to give the squared *rms* fractional variability per Hertz.

To have the timing evolution of QPO features in different classes, we generate PCA light curves of 2 to 40keV photons with 0.01s time bin. We use the science data accordingly from the ‘binned mode’ and the ‘event mode’ for 10s time interval in each step. This light curve is then used to make PDS

| Obs-Id | Class | Date |
|-----------------|-------------------|------------|
| 10408-01-19-00* | I (ϕ) | 29-06-1996 |
| 10408-01-09-00 | I (ϕ) | 29-05-1996 |
| 10408-01-18-00* | II (δ) | 25-06-1996 |
| 20402-01-41-00 | II (δ) | 19-08-1997 |
| 20402-01-37-00* | III (γ) | 17-07-1997 |
| 20402-01-56-00 | III (γ) | 22-11-1997 |
| 40703-01-27-00* | IV (ω) | 23-08-1999 |
| 40403-01-07-00 | IV (ω) | 23-04-1999 |
| 10408-01-36-00* | V (μ) | 28-09-1996 |
| 20402-01-53-01 | V (μ) | 05-11-1997 |
| 10408-01-40-00* | VI (ν) | 13-10-1996 |
| 20402-01-02-02 | VI (ν) | 14-11-1996 |
| 20402-01-36-00* | VII (λ) | 10-07-1997 |
| 10408-01-38-00 | VII (λ) | 07-10-1996 |
| 20402-01-33-00* | VIII (κ) | 18-06-1997 |
| 20402-01-35-00 | VIII (κ) | 07-07-1997 |
| 20402-01-03-00* | IX (ρ) | 03-06-1997 |
| 20402-01-31-00 | IX (ρ) | 19-11-1996 |
| 80127-01-02-00* | X (ξ) | 2003-03-07 |
| 10408-01-10-00* | XI (β) | 26-05-1996 |
| 20402-01-44-00 | XI (β) | 31-08-1997 |
| 20187-02-01-00* | XII (α) | 07-05-1997 |
| 20402-01-30-01 | XII (α) | 28-05-1997 |
| 10408-01-15-00* | XIII (θ) | 16-06-1996 |
| 20402-01-45-02 | XIII (θ) | 05-09-1997 |
| 20402-01-16-00* | XIV (χ_2) | 22-02-1997 |
| 20402-01-05-00 | XIV (χ_2) | 04-12-1996 |
| 20402-01-25-00* | XV (χ_4) | 19-04-1997 |
| 10408-01-33-00 | XV (χ_4) | 07-09-1996 |
| 10408-01-23-00* | XVI (χ_1) | 14-07-1996 |
| 10408-01-30-00 | XVI (χ_1) | 18-08-1996 |
| 20402-01-50-00* | XVII (χ_3) | 14-10-1997 |
| 20402-01-51-00 | XVII (χ_3) | 22-10-1997 |

Table 1: The ObsIDs and the dates of the RXTE data analyzed in this paper. * represents the result shown in Fig. 3 of this paper.

using the `powspec` task. The dynamic PDS is made by considering the shift of time interval by 1s. The selection of time interval is done by FTOOLS task ‘`timetrans`’. The PDSs are plotted accordingly to see the variation of QPO features in a particular class of a few hundred seconds of observation.

2.2. Spectral Analysis

Spectral analysis of the PCA data is done by using “standard2” mode data which have 16 sec time resolution and we constrained our energy selection up to 40 keV to match with the timing analysis. The source spectrum is generated using FTOOLS task “SAEXTRACT” with 16 sec time bin from “standard2” data. The background fits file is generated from the “standard2” fits file by the FTOOLS task “`runpcabackest`” with the standard FILTER file provided with the package. The background source spectrum is generated using FTOOLS task “SAEXTRACT” with 16 sec time bin from background fits file. The standard FTOOLS task “`pcarsp`” is used to generate the response file with appropriate detector information. The spectral analysis and modeling was performed using XSPEC (v.12) astrophysical fitting package. For the model fitting of the PCA spectra, we have used a systematic error of 0.5%. The spectra are fitted with diskbb and power-law model along with $6.0 \times 10^{22} \text{cm}^{-2}$ hydrogen column absorption (Muno et al., 1999) and we used the Gaussian for iron line as required for the best fitting. Morrison et al. (1983) reported that mainly affects the photons from 0.03 to 10.0 keV. It is important to consider hydrogen column absorption for RXTE analysis because 2.0 – 10.0 keV photons contain several informations. As we are interested about the changes in the frame of the compact object we have chosen the n_H carefully. While choosing the model to extract the number of photons, we need to be careful. First of all, one single model must be able to fit spectra of all the seventeen classes with sufficient accuracy, otherwise, the comparison of the Comptonization efficiency becomes meaningless. Second: the model must have the flexibility to provide soft-photons in a dynamically obtained energy band, the limit of which is to be determined automatically so as to get the best χ^2 . While there are a number of models in the literature such as ComptST, SIMPL etc., we adopt the method used by Sobczak et al. (1999) to obtain the spectral parameters as it satisfies both the criteria mentioned above. We also point out that at this stage, we do not consider the effects of hardening factor (Shimura et al., 1995) arising out of Comptonization by an optically thin haze over the accretion disk. In Figs. 1(a-b), we present an example (Obs. ID 20402-01-16-00) of why Sobczak et al. (1999)

is useful in our context. Both the Figures represent the analysis of the same spectrum of a data in XIV class. In Fig. 1(a), the spectrum is fitted by the standard method with the *diskbb* and power-law model. From this unfolded spectrum, it is observed that the *diskbb* component is weaker than the power-law component. However, if we try to fit this spectrum only with a power-law component then similar fitting parameters are also obtained and the χ^2 value remained similar. So the ratio of the power-law photon number to *diskbb* photon number would have no meaning. On the contrary, in Fig. 1(b), we fit the spectrum with the [Sobczak et al. \(1999\)](#) method. This gives a similar χ^2 and the unfolded spectrum is shown. The ratio CE is calculable without any confusion. The results of the analysis of all the classes using this method are given in Table 2 & 3 which will be described later. We have verified that for the intermediate classes, the parameters obtained from both the fitting methods remain similar. However, since in the present paper, we are dealing with all the variability classes with a significant spectral difference, we adopted the method of [Sobczak et al. \(1999\)](#) to analyze all the classes using a single procedure. Another advantage of this method is that we can compute the upper limit of energy dbb_e to be used for the *diskbb* model dynamically in every time bin of the spectrum and thus obtained the dynamical hardness ratio, i.e., the Comptonization efficiency, CE. We have obtained dbb_e by fitting the spectrum with *diskbb* only and changing the upper energy limit E_{fit} till we have a $\tilde{\chi}^2$ value ≈ 1 . This yields $dbb_e = E_{fit}$. From Tables 2 & 3, we see the variation of dbb_e for all the classes. In Table 2, (which is for *diskbb* plus power-law model) the column 1 gives the variability class with 'h' and 's' representing the harder (burst-off) and softer (burst-on) states respectively. Columns 2 and 3 give the black body temperature and the upper energy limit dbb_e obtained from the fit. Column 4 gives the $\chi^2(dof)$ for the *diskbb* spectral model fitting. Column 5 gives the number of blackbody photons between dbb_e and 0.1keV. Column 6 gives the power-law index. Column 7 contains the number of Comptonized photons in the range of $3 \times T_{in}$ to 40keV. Last two columns give the Comptonizing efficiency CE and the $\chi^2(dof)$ higher energy range. Table 3 is for *diskbb* plus *ComptST* model. Here, most of the columns have the same meaning as in Table 2. However, instead of the power-law index α , we presented the electron temperature T_e and the optical depth τ . Note that it is not always possible to fit with the *COMPST* model. Hence some of the rows in Table 3 do not have entries. We have calculated error-bars at 90% confidence level in each case.

To have the spectral evolution with time for each class, we have generated

the PCA spectrum (2.0 to 40keV) with a minimum of 16s time interval along with the background spectrum and response matrix. This procedure is repeated with every 16s shift in time interval since the minimum time resolution in ‘standard2’ data is 16s. We use ‘timetrans’ task to select each step of time interval. Spectral evolution (dynamic representation) for a longer duration of observation (~ 500 to 2000 sec) of each class is plotted to show the local spectral variation in each class.

3. Calculation Procedure

In this Section, we discuss the process of calculation of photon numbers using the parameters obtained from the spectral fit.

We fit each spectrum in XSPEC environment using the models and the constraints mentioned earlier. The fitting parameters are used to calculate the black body photons from the standard disk and the power-law photons from the Compton cloud. The number of black body photons are obtained from the fitted parameters of the multi-color disk black body model (Makishima et al., 1986). This is given by,

$$f(E) = \frac{8\pi}{3} r_{in}^2 \cos i \int_{T_{out}}^{T_{in}} (T/T_{in})^{-11/3} B(E, T) dT/T_{in}, \quad (1)$$

where, $B(E, T) = \frac{E^3}{(\exp E/T - 1)}$ and r_{in} can be calculated from,

$$K = (r_{in}/(D/10kpc))^2 \cos i, \quad (2)$$

where, K is the normalization of the blackbody spectrum obtained after fitting, r_{in} is the inner radius of the accretion disk in km , T_{in} is the temperature at r_{in} in keV, D is the distance of the compact object in kpc and i is the inclination angle of the accretion disk. Here, both the energy and the temperature are in keV. The black body flux, $f(E)$ in photons/s/keV is integrated between 0.1 keV to the maximum energy dbb_e . This gives us γ_{BB} , the rate of the number of the emitted black body photons.

The Comptonized photons γ_{PL} that are produced due to inverse-Comptonization of the soft black body photons by ‘hot’ electrons in the Compton cloud are calculated by fitting with the power-law given below,

$$P(E) = N(E)^{-\alpha}, \quad (3)$$

where, α is the power-law index and N is the total *photons/s/cm²/keV* at 1keV. It is reported in [Titarchuk \(1994\)](#), that the Comptonization spectrum will have a peak at around $3 \times T_{in}$. The power law equation is integrated from $3 \times T_{in}$ to 40keV to obtain the rate of emitted Comptonized photons. The Gaussian function $Ga(E)$ is incorporated with a power-law equation for the presence of line emissions in the spectrum, whenever necessary is given below,

$$Ga(E) = L \left(\frac{1}{\sigma\sqrt{2\pi}} \right) \exp \left(-0.5 \left(\frac{E - E_l}{\sigma} \right)^2 \right), \quad (4)$$

where, E_l is the energy of emitted line in keV, σ is the line width in keV and L is the total number of *photons/s/cm²* in the line. The variation of the Comptonizing Efficiency (CE) with time is plotted to have an idea of how the Compton cloud may be changing its geometry.

Just for comparison, we tried to fit the data with another Comptonization model, namely, the *compST* ([Sunyaev et al., 1980](#)). The spectrum is given by,

$$\begin{aligned} Cst(x) &= \frac{\alpha(\alpha+3)}{2\alpha+3} \left(\frac{x}{x_0} \right)^{\alpha+3}, \text{ when } 0 \leq x \leq x_0, \\ &= \frac{\alpha(\alpha+3)x_0^\alpha}{\Gamma(2\alpha+4)} x^3 \exp(-x) I(x), \text{ when } x \geq x_0. \end{aligned} \quad (5)$$

Here, $I(x) = \int_0^\infty t^{\alpha-1} \exp -t \left(1 + \frac{t}{x} \right)^{\alpha+3}$, $x = E/kT_e$, $x_0 = kT_{in}/kT_e$ and α is the spectral index. This α is calculated from $\alpha = \sqrt{\frac{9}{4} + \gamma} - \frac{3}{2}$, where $\gamma = \frac{\pi^2 m_e c^2}{3(\tau + \frac{2}{3})^2 kT_e}$. kT_e is the electron temperature and τ is the optical depth of the electron cloud. In the computation, we exclude the hydrogen column absorption feature while calculating CE. This is because we are interested in the photons which were emitted from the disk before suffering any absorption. Thus the variation of CE along with other features (e.g., spectral and QPO frequency variations) will reflect the *actual* radiative properties of the flow near a black hole.

In Figs. 1(c-d), we show the PCA and HEXTE spectrum of the data of the same Obs. ID (20402-01-33-00) along with the fitted components. We also show the residuals to characterize the goodness of the fit. In Fig. 1(c), the fitting is done with *diskbb* and power-law components. The photon numbers and CE are calculated with the parameters obtained from the fitting. The

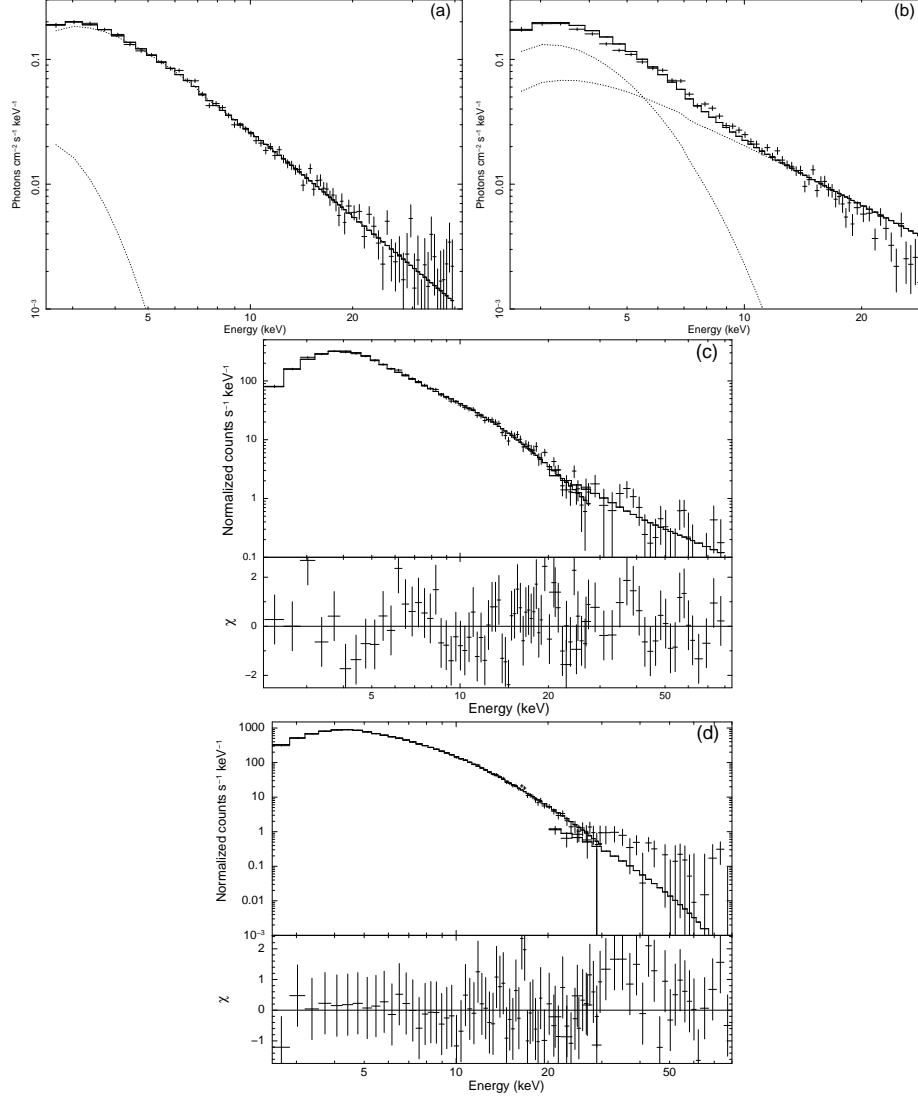


Figure 1: (a) The unfolded PCA spectrum of a data (Obs. ID 20402-01-16-00) fitted with the *diskbb* and power-law with the standard method. (b) The unfolded PCA spectrum of (a) fitted with *diskbb* and power-law with the Sobczak et al. (1999) method. (c) The fitted spectrum of PCA & HEXTE data (Obs. ID 20402-01-33-00) along with the *diskbb* and power-law components. (d) The PCA & HEXTE sample spectrum of (c) fitted with *diskbb* and *compST* components.

black body photons are calculated with $T_{in} = 1.15^{+0.06}_{-0.05}$ keV. Here the $\tilde{\chi}^2$ is 1.1 with 10 degrees of freedoms. The calculated number of black body photons from 0.1 – 6.5keV is $156.03^{+17.10}_{-13.90}$ kphotons/s. In the same way, the power-law photons are calculated with the power-law index = $2.06^{+0.15}_{-0.15}$. The calculated number of the Comptonized photons between 3.45 – 40 keV is $0.39^{+0.06}_{-0.05}$ kphotons/s. The ratio between the power-law photon and the black body photon is $0.25^{+0.08}_{-0.07}\%$. This means that only 0.25% of the soft photons are Comptonized by the Compton cloud. In Fig. 1(c), we also include HEXTE data, and fitted with a power-law. But the spectral fit does not change in slope and the number of photons contributed by HEXTE region is so low that the value of CE remains unchanged. In Fig. 1(d), the same spectrum is fitted with *diskbb* and *compST* models. The calculation with the *compST* model parameters are found to be $kT_e = 6.41^{+2.55}_{-1.25}$ and $\tau = 9.42^{+2.88}_{-2.39}$. The number of Comptonized photons within the same range as in Fig. 1(c) is $0.41^{+0.06}_{-0.05}$ kphotons/s. Thus the ratio between the *compST* photon and the *diskbb* photon is $0.26^{+0.08}_{-0.07}\%$. In case of harder states the both PCA and HEXTE analysis give similar model parameters at the higher energies. In case of softer states the higher energy region data has bigger error bars. This is true for several variability classes. We therefore ignore the HEXTE data in the rest of the paper to keep the analysis procedure similar for all the variability classes. It is to be noted that there is a scope of possible double counting of a very few photons in the region where the blackbody and power-law components overlaps. We have verified that this does not amount to a change of more than 0.3% in CE.

Steiner et al. (2011) presented an empirical model of Comptonization for fitting the spectra “SIMPL”. This package has been implemented in XSPEC. We have carried out our fitting by using this model also. The value of Γ (photon power-law index) has been found to be nearly equal (within errorbars) to the power-law index we obtained from using power-law model. The scattered fraction parameter *FracSctr* of this model gives the amount of black body photons Comptonized by the electron cloud. If we calculate CE within a specific energy range (say 2 – 40keV) we get a similar value as *FracSctr* parameter. However, we are not only interested in the 2 – 40keV range, but also in the range in which the data is not obtained by RXTE. That is to say, we like to put ourselves in the frame of the disk, and not in the frame of the observer. Thus, for an accurate CE, we must have the photon rates from lower energy range of 0.1 – 2keV as well. That is why we choose to follow our procedure rather than using SIMPL model.

In several of the classes, we see that the photon numbers have two distinct states (see, [Chakrabarti et al. \(2002\)](#) and references therein): one in which the count is lower (burst-off state designated as ‘h’ in Tables 2 and 3) and the other in which the count is higher (burst-on state designated as ‘s’ in Tables 2 and 3).

In Table 2, a comparison of the fitted parameters for a sample single 16s bin for all the classes are provided with an error at 90% confidence level. Just to compare, we fit the spectrum of each class with the *diskbb* and *compST* model to have the information of τ and T_e of electron distribution inside the Compton cloud. The same sample 16s bin spectrum which were analyzed in Table 2 is taken for each class and fitted with the *diskbb* and *compST* model with $n_H = 6.0 \times 10^{22} \text{ cm}^{-2}$ hydrogen column for absorption and 0.5% as the systematic error. The best fitted parameters are given in Table 3 for comparison. We find that in the cases where both models were satisfactory, the CE obtained were very close to each other. So our result appears to be model independent.

4. Results

We discuss below the main results for each class. The Observational IDs are given in Table 1. So far, we showed that the value of CE, averaged over a class, varies from one variability class to another. We now present the results of the dynamical analysis of the light curves of all the variability classes. While choosing the data duration for a given class, the following considerations have been made: If the count rate has no obvious high and low count features, we use the data of 500s. If the count rates have some ‘repetitive’ behavior, we use the data of 500, 1000, 1500s or even 2000s, which ever is bigger so that at least one full cycle is included in the chunk of the data. However, in the latter cases, while computing the average value of CE, we use the data from a full cycle only.

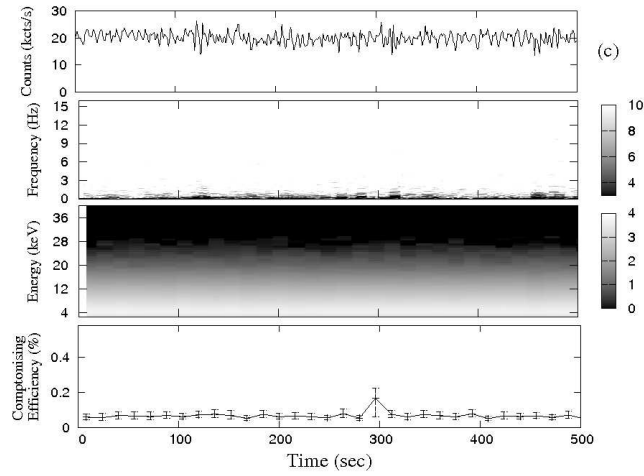
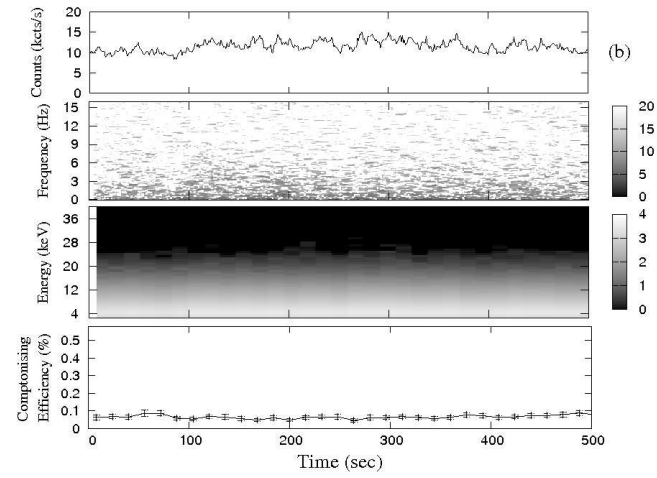
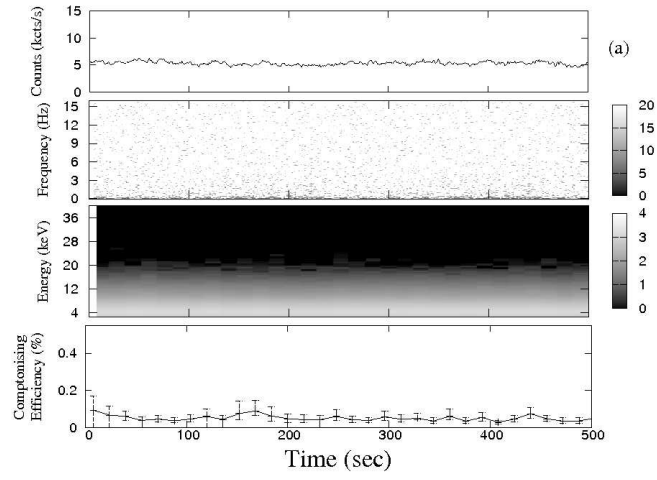
In each of Figs. 2(a-q) we show four panels. The top panel is the variation of the photons with time. The second panel is the variation of $\log(\text{power})$ of the dynamical Power Density Spectra (PDS) which may show presence or absence of quasi-periodic variations or QPOs. The third panel is the dynamic energy spectrum which shows whether the variability class is dominated by power-law photons or black-body photons. Finally, the bottom panel shows the variation of Comptonizing Efficiency CE calculated using 16 seconds of binned data. The error bar is provided at the 90% confidence level.

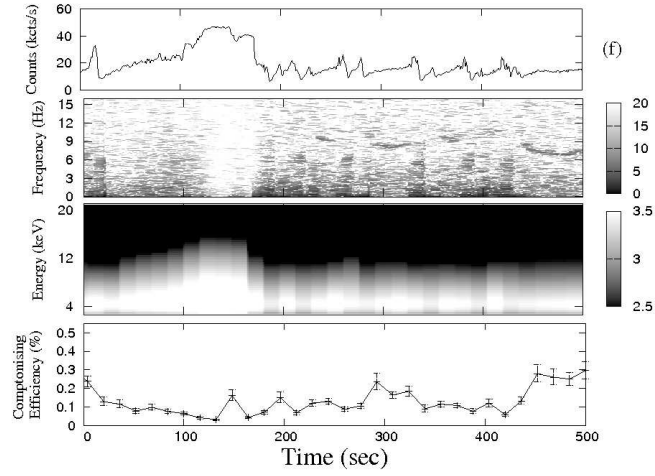
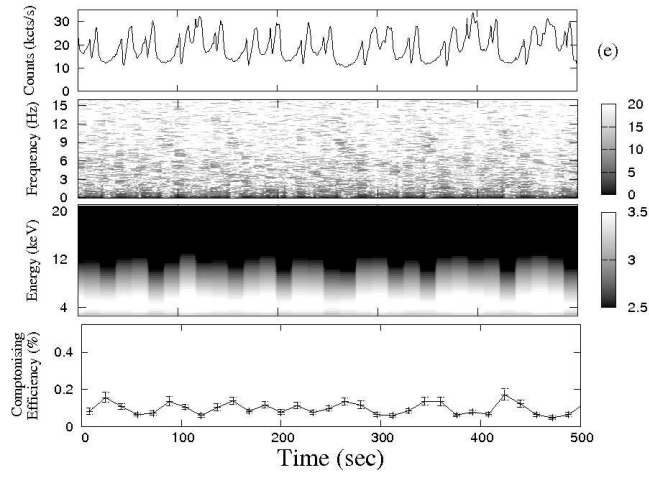
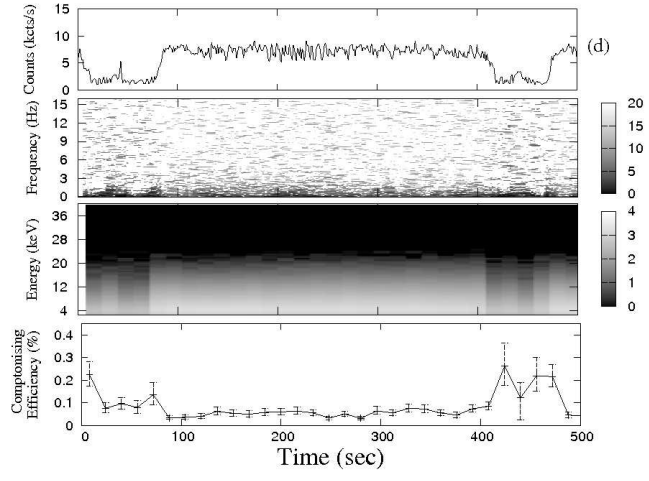
| Class | | T_{in} (keV) | dbb_e (keV) | $\bar{\chi}^2$ (dofs) | Soft Photon (kphtns/s) | Power law index | Hard Photon (kphtns/s) | CE (%) | $\bar{\chi}^2$ (dofs) |
|------------------|---|--|------------------|--------------------------|--|--|--|--|--------------------------|
| I(ϕ) | - | 1.67 ^{+0.02} _{-0.02} | 10.2 | 1.2(18) | 275.08 ^{+8.77} _{-8.46} | 2.93 ^{+0.27} _{-0.26} | 0.20 ^{+0.04} _{-0.03} | 0.07 ^{+0.02} _{-0.01} | 1.6(70) |
| II(δ) | - | 1.65 ^{+0.02} _{-0.01} | 10.3 | 1.5(17) | 330.40 ^{+9.48} _{-9.80} | 2.35 ^{+0.24} _{-0.23} | 0.16 ^{+0.03} _{-0.02} | 0.05 ^{+0.01} _{-0.01} | 1.1(69) |
| III(γ) | - | 1.80 ^{+0.01} _{-0.01} | 10.4 | 1.2(17) | 511.13 ^{+12.57} _{-12.22} | 2.92 ^{+0.35} _{-0.31} | 0.31 ^{+0.09} _{-0.07} | 0.06 ^{+0.02} _{-0.01} | 1.5(58) |
| IV(ω) | - | 1.94 ^{+0.02} _{-0.02} | 10.6 | 1.1(15) | 192.21 ^{+7.80} _{-7.41} | 2.65 ^{+0.31} _{-0.29} | 0.09 ^{+0.02} _{-0.01} | 0.05 ^{+0.01} _{-0.01} | 1.0(54) |
| V(μ) | - | 1.42 ^{+0.02} _{-0.02} | 7.0 | 1.5(10) | 468.53 ^{+10.40} _{-10.02} | 2.33 ^{+0.14} _{-0.14} | 0.63 ^{+0.08} _{-0.07} | 0.13 ^{+0.02} _{-0.02} | 1.0(66) |
| VI(ν) | - | 1.75 ^{+0.03} _{-0.03} | 7.0 | 1.7(10) | 370.39 ^{+14.15} _{-13.15} | 2.58 ^{+0.12} _{-0.12} | 0.45 ^{+0.04} _{-0.03} | 0.12 ^{+0.02} _{-0.01} | 1.2(69) |
| VII(λ) | h | 0.93 ^{+0.06} _{-0.05} | 4.5 | 1.4(7) | 229.10 ^{+28.94} _{-22.32} | 2.11 ^{+0.12} _{-0.11} | 0.59 ^{+0.07} _{-0.06} | 0.26 ^{+0.08} _{-0.07} | 0.9(59) |
| | s | 1.99 ^{+0.02} _{-0.02} | 9.0 | 1.1(14) | 437.22 ^{+11.11} _{-10.62} | 2.68 ^{+0.22} _{-0.21} | 0.19 ^{+0.3} _{-0.2} | 0.04 ^{+0.01} _{-0.01} | 1.2(69) |
| VIII(κ) | h | 1.15 ^{+0.06} _{-0.05} | 6.5 | 1.4(10) | 156.03 ^{+17.10} _{-13.90} | 2.06 ^{+0.15} _{-0.15} | 0.39 ^{+0.06} _{-0.05} | 0.25 ^{+0.08} _{-0.07} | 1.2(60) |
| | s | 1.90 ^{+0.03} _{-0.03} | 8.0 | 0.9(11) | 432.72 ^{+13.95} _{-13.15} | 2.98 ^{+0.24} _{-0.23} | 0.21 ^{+0.03} _{-0.03} | 0.05 ^{+0.01} _{-0.01} | 1.5(51) |
| IX(ρ) | h | 1.38 ^{+0.03} _{-0.03} | 5.7 | 1.6(8) | 382.33 ^{+18.42} _{-16.73} | 2.50 ^{+0.10} _{-0.10} | 0.95 ^{+0.09} _{-0.08} | 0.25 ^{+0.04} _{-0.03} | 1.5(52) |
| | s | 1.84 ^{+0.02} _{-0.02} | 8.0 | 1.7(11) | 419.92 ^{+11.55} _{-10.97} | 2.33 ^{+0.16} _{-0.15} | 0.34 ^{+0.04} _{-0.03} | 0.08 ^{+0.01} _{-0.01} | 1.0(55) |
| X(ξ) | h | 1.14 ^{+0.05} _{-0.04} | 5.5 | 0.8(11) | 162.63 ^{+21.83} _{-18.49} | 2.82 ^{+0.19} _{-0.18} | 0.33 ^{+0.11} _{-0.09} | 0.20 ^{+0.08} _{-0.10} | 1.1(52) |
| | s | 1.39 ^{+0.02} _{-0.02} | 9.5 | 1.3(13) | 106.38 ^{+5.83} _{-5.50} | 2.41 ^{+0.48} _{-0.44} | 0.07 ^{+0.09} _{-0.04} | 0.06 ^{+0.02} _{-0.01} | 1.1(55) |
| XI(β) | h | 1.04 ^{+0.03} _{-0.03} | 5.2 | 1.0(10) | 320.15 ^{+20.78} _{-18.15} | 2.14 ^{+0.06} _{-0.06} | 0.87 ^{+0.05} _{-0.04} | 0.27 ^{+0.04} _{-0.04} | 1.1(69) |
| | s | 1.45 ^{+0.02} _{-0.02} | 7.0 | 1.5(12) | 354.87 ^{+12.38} _{-11.58} | 2.69 ^{+0.18} _{-0.17} | 0.32 ^{+0.05} _{-0.04} | 0.14 ^{+0.03} _{-0.03} | 1.6(60) |
| XII(α) | - | 1.21 ^{+0.08} _{-0.07} | 4.5 | 1.1(8) | 261.36 ^{+38.46} _{-28.74} | 2.07 ^{+0.06} _{-0.06} | 0.81 ^{+0.04} _{-0.04} | 0.31 ^{+0.08} _{-0.07} | 1.0(65) |
| XIII(θ) | h | 1.39 ^{+0.04} _{-0.04} | 6.0 | 1.3(10) | 416.84 ^{+25.73} _{-22.85} | 2.50 ^{+0.09} _{-0.09} | 1.15 ^{+0.09} _{-0.08} | 0.28 ^{+0.05} _{-0.04} | 1.6(58) |
| | s | 1.32 ^{+0.03} _{-0.03} | 5.5 | 1.6(10) | 388.95 ^{+21.46} _{-19.19} | 3.25 ^{+0.16} _{-0.15} | 0.65 ^{+0.08} _{-0.07} | 0.17 ^{+0.03} _{-0.03} | 1.5(63) |
| XIV(χ_2) | - | 1.20 ^{+0.12} _{-0.09} | 4.5 | 1.1(6) | 126.80 ^{+27.74} _{-18.46} | 1.97 ^{+0.08} _{-0.07} | 0.57 ^{+0.03} _{-0.03} | 0.45 ^{+0.17} _{-0.12} | 1.6(60) |
| XV(χ_4) | - | 1.18 ^{+0.11} _{-0.09} | 4.5 | 1.2(6) | 121.04 ^{+25.87} _{-17.37} | 1.95 ^{+0.08} _{-0.08} | 0.52 ^{+0.03} _{-0.02} | 0.43 ^{+0.16} _{-0.12} | 1.4(60) |
| XVI(χ_1) | - | 1.16 ^{+0.05} _{-0.05} | 4.5 | 1.4(6) | 599.39 ^{+38.18} _{-47.51} | 2.74 ^{+0.06} _{-0.06} | 4.62 ^{+0.12} _{-0.11} | 0.77 ^{+0.08} _{-0.07} | 1.7(57) |
| XVII(χ_3) | - | 1.19 ^{+0.03} _{-0.03} | 5.0 | 1.3(6) | 598.83 ^{+31.99} _{-28.57} | 2.70 ^{+0.06} _{-0.06} | 5.30 ^{+0.09} _{-0.09} | 0.88 ^{+0.10} _{-0.09} | 1.3(61) |

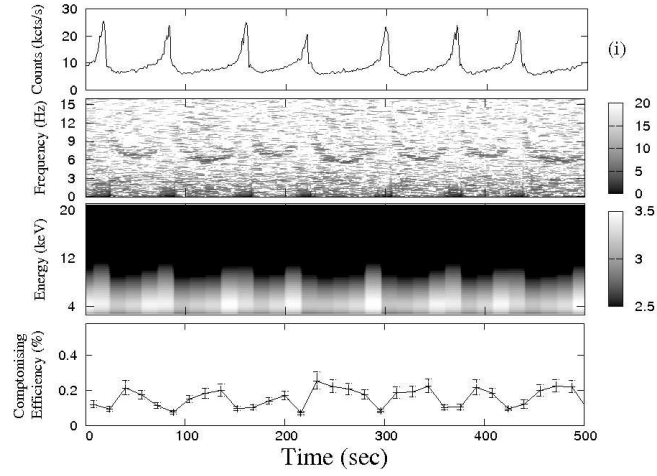
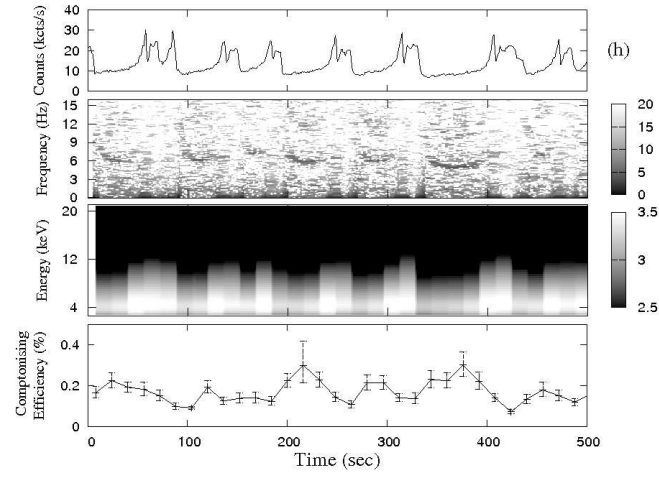
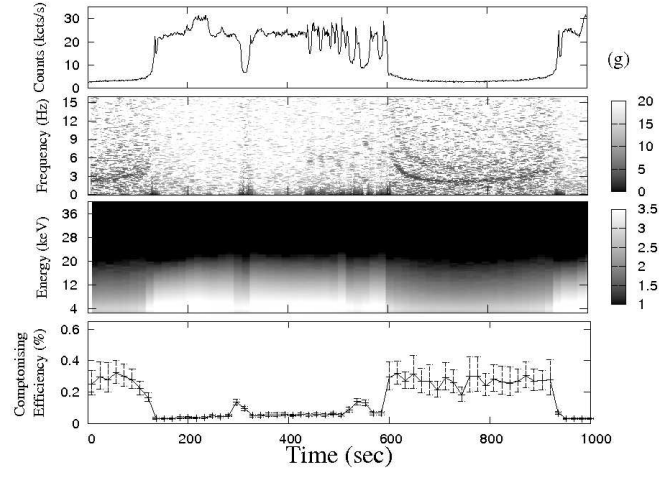
Table 2: Parameters for the spectral fits of sample single 16s bin with *diskbb* plus *powerlaw* models for all the variability classes. T_{in} is the black body temperature obtained from fitting. dbb_e is the upper limit of the disk blackbody spectrum. The column containing the soft photon rate contains blackbody photons in the $0.1 - dbb_e$ keV. The column ‘power-law’ contains the power-law index α obtained from fitting. The column ‘hard photons’ contains the rate at which Comptonized photons are emitted in the range $3 \times T_{in} - 40$ keV. CE is the Comptonized efficiency.

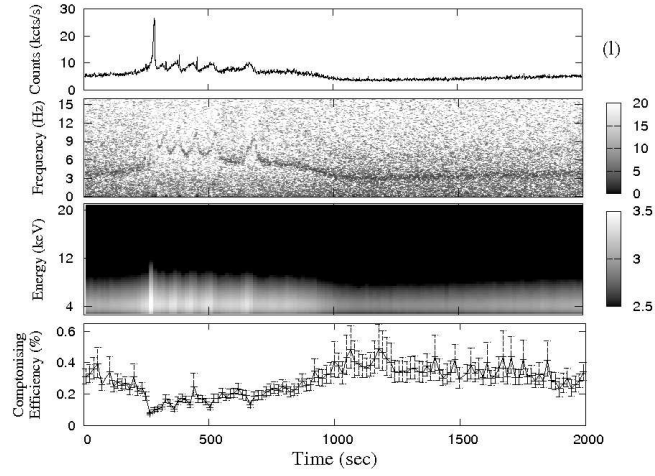
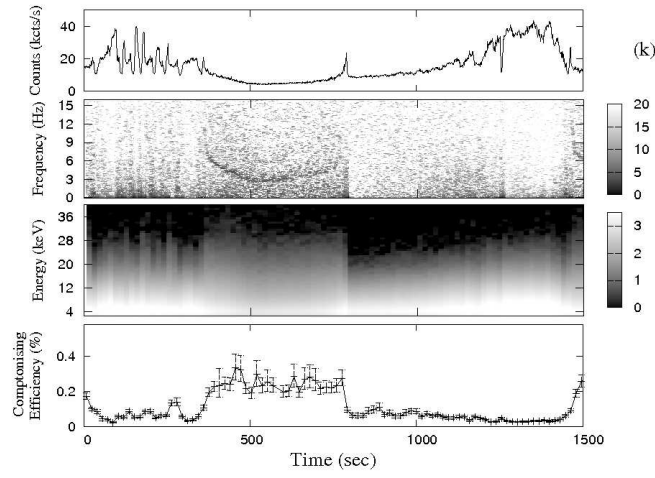
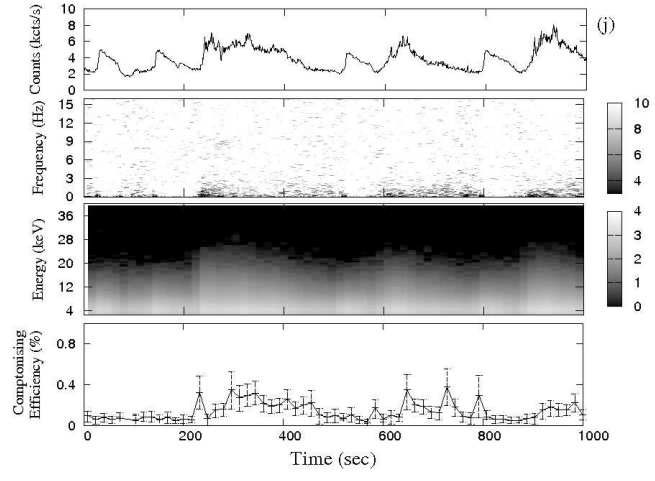
| Class | | T_{in} (keV) | dbb_e (keV) | $\bar{\chi}^2$ (dofs) | Soft Photon (kphotons/sec) | T_e keV | τ | Hard Photon (kphotons/s) | CE (%) | $\bar{\chi}^2$ (dofs) |
|-------|---|-------------------------|------------------|--------------------------|----------------------------------|-------------------------|---------------------------|--------------------------------|-------------------------|--------------------------|
| I | - | 1.67 $^{+0.02}_{-0.02}$ | 10.2 | 1.2(18) | 275.08 $^{+8.77}_{-8.46}$ | - | - | - | - | - |
| II | - | 1.65 $^{+0.02}_{-0.01}$ | 10.3 | 1.5(17) | 330.04 $^{+9.48}_{-9.80}$ | - | - | - | - | - |
| III | - | 1.80 $^{+0.01}_{-0.01}$ | 10.4 | 1.2(17) | 511.13 $^{+12.57}_{-12.22}$ | - | - | - | - | - |
| IV | - | 1.94 $^{+0.02}_{-0.02}$ | 10.6 | 1.1(15) | 192.21 $^{+7.80}_{-7.41}$ | - | - | - | - | - |
| V | - | 1.42 $^{+0.02}_{-0.02}$ | 7.0 | 1.5(10) | 468.53 $^{+10.40}_{-10.02}$ | 4.72 $^{+0.98}_{-0.66}$ | 14.40 $^{+4.62}_{-4.46}$ | 0.61 $^{+0.08}_{-0.07}$ | 0.13 $^{+0.02}_{-0.02}$ | 1.0(61) |
| VI | - | 1.75 $^{+0.03}_{-0.03}$ | 7.0 | 1.7(10) | 370.39 $^{+14.15}_{-13.15}$ | - | - | - | - | - |
| VII | h | 0.93 $^{+0.06}_{-0.05}$ | 4.5 | 1.4(7) | 229.10 $^{+28.94}_{-22.32}$ | 4.93 $^{+1.08}_{-0.68}$ | 12.43 $^{+2.75}_{-2.25}$ | 0.52 $^{+0.07}_{-0.06}$ | 0.22 $^{+0.08}_{-0.07}$ | 1.5(60) |
| | s | 1.99 $^{+0.02}_{-0.02}$ | 9.0 | 1.1(14) | 437.22 $^{+11.11}_{-10.62}$ | - | - | - | - | - |
| VIII | h | 1.15 $^{+0.06}_{-0.05}$ | 6.5 | 1.4(10) | 156.03 $^{+17.10}_{-13.90}$ | 6.41 $^{+2.56}_{-1.25}$ | 9.41 $^{+2.88}_{-2.39}$ | 0.41 $^{+0.06}_{-0.05}$ | 0.26 $^{+0.08}_{-0.07}$ | 0.9(58) |
| | s | 1.90 $^{+0.03}_{-0.03}$ | 8.0 | 0.9(11) | 437.72 $^{+13.95}_{-13.15}$ | - | - | - | - | - |
| IX | h | 1.38 $^{+0.03}_{-0.03}$ | 5.7 | 1.6(8) | 382.33 $^{+18.42}_{-16.73}$ | 3.89 $^{+0.46}_{-0.29}$ | 30.93 $^{+4.36}_{-4.36}$ | 0.75 $^{+0.09}_{-0.08}$ | 0.20 $^{+0.04}_{-0.03}$ | 1.4(61) |
| | s | 1.84 $^{+0.02}_{-0.02}$ | 8.0 | 1.7(11) | 419.92 $^{+11.55}_{-10.97}$ | - | - | - | - | - |
| X | h | 1.14 $^{+0.05}_{-0.04}$ | 5.5 | 0.8(11) | 162.63 $^{+21.83}_{-18.49}$ | 3.19 $^{+1.15}_{-0.59}$ | 14.36 $^{+27.70}_{-5.72}$ | 0.29 $^{+0.09}_{-0.08}$ | 0.17 $^{+0.05}_{-0.06}$ | 0.8(58) |
| | s | 1.39 $^{+0.02}_{-0.02}$ | 9.5 | 1.3(13) | 106.38 $^{+5.83}_{-5.50}$ | - | - | - | - | - |
| XI | h | 1.04 $^{+0.03}_{-0.03}$ | 5.2 | 1.0(10) | 320.15 $^{+20.78}_{-18.15}$ | 4.61 $^{+0.82}_{-0.56}$ | 11.07 $^{+2.88}_{-2.10}$ | 0.57 $^{+0.05}_{-0.04}$ | 0.18 $^{+0.04}_{-0.04}$ | 0.9(56) |
| | s | 1.45 $^{+0.02}_{-0.02}$ | 7.0 | 1.5(12) | 354.87 $^{+12.58}_{-11.58}$ | - | - | - | - | - |
| XII | - | 1.21 $^{+0.08}_{-0.07}$ | 4.5 | 1.1(8) | 261.36 $^{+38.46}_{-28.74}$ | 5.04 $^{+0.51}_{-0.41}$ | 11.91 $^{+1.54}_{-1.32}$ | 0.71 $^{+0.04}_{-0.04}$ | 0.27 $^{+0.08}_{-0.07}$ | 1.4(58) |
| XIII | h | 1.39 $^{+0.04}_{-0.04}$ | 6.0 | 1.3(10) | 416.84 $^{+25.73}_{-22.85}$ | 4.13 $^{+0.67}_{-0.47}$ | 14.41 $^{+1.49}_{-4.10}$ | 0.96 $^{+0.09}_{-0.08}$ | 0.43 $^{+0.07}_{-0.07}$ | 1.3(64) |
| | s | 1.32 $^{+0.03}_{-0.03}$ | 5.5 | 1.6(10) | 388.95 $^{+21.46}_{-19.19}$ | - | - | - | - | - |
| XIV | - | 1.20 $^{+0.12}_{-0.09}$ | 4.5 | 1.1(6) | 126.80 $^{+27.74}_{-18.46}$ | 8.92 $^{+1.95}_{-2.30}$ | 6.80 $^{+1.93}_{-2.64}$ | 0.52 $^{+0.03}_{-0.03}$ | 0.41 $^{+0.17}_{-0.12}$ | 1.5(61) |
| XV | - | 1.18 $^{+0.11}_{-0.09}$ | 4.5 | 1.2(6) | 121.04 $^{+25.87}_{-17.37}$ | 6.62 $^{+2.74}_{-1.23}$ | 8.79 $^{+2.22}_{-2.15}$ | 0.51 $^{+0.03}_{-0.02}$ | 0.42 $^{+0.16}_{-0.12}$ | 0.90(60) |
| XVI | - | 1.16 $^{+0.05}_{-0.05}$ | 4.5 | 1.4(6) | 599.39 $^{+58.18}_{-47.51}$ | 4.64 $^{+0.82}_{-0.55}$ | 8.50 $^{+1.58}_{-1.40}$ | 4.10 $^{+0.12}_{-0.11}$ | 0.68 $^{+0.08}_{-0.07}$ | 1.3(62) |
| XVII | - | 1.19 $^{+0.03}_{-0.03}$ | 5.0 | 1.3(6) | 598.83 $^{+31.99}_{-28.57}$ | 6.62 $^{+2.74}_{-1.23}$ | 8.79 $^{+2.22}_{-2.15}$ | 5.20 $^{+0.09}_{-0.09}$ | 0.87 $^{+0.10}_{-0.09}$ | 1.2(60) |

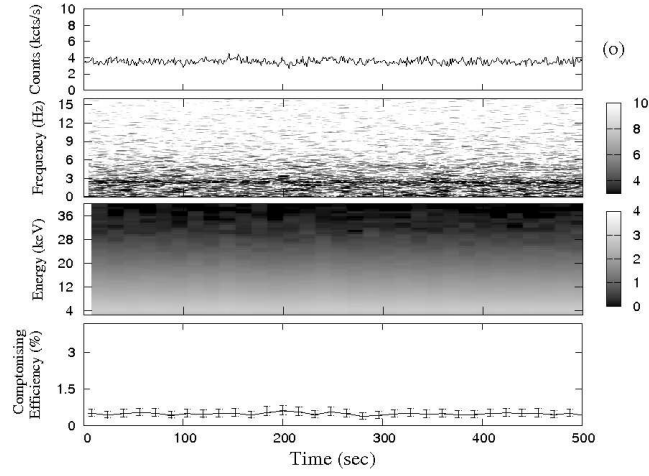
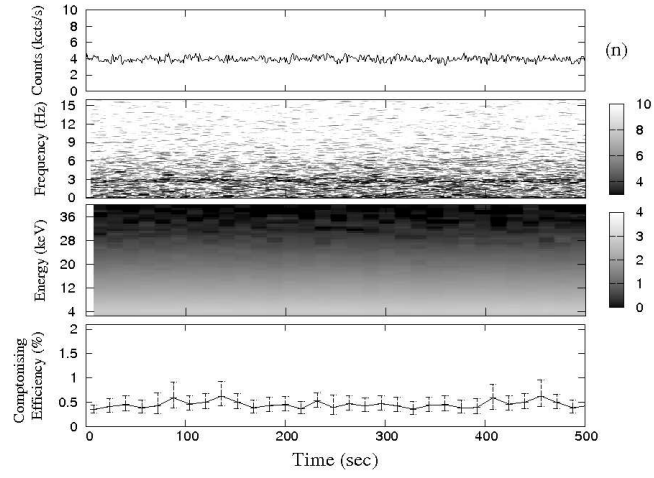
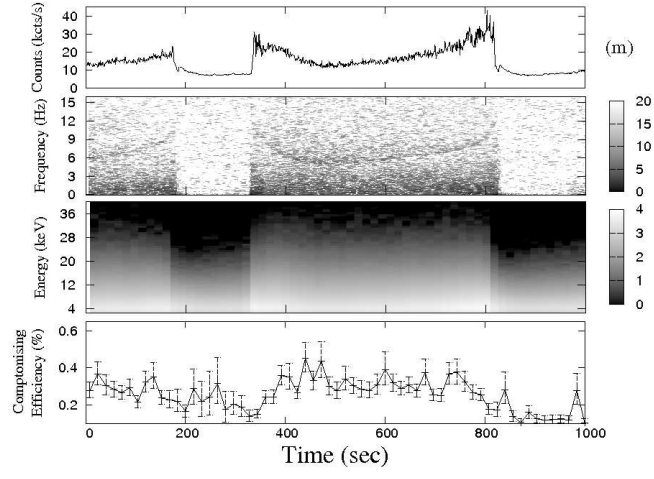
Table 3: Same data as in Table 2, analyzed with the *diskbb* and *comptST* model. Most of the columns have the same meaning as in Table 2. However, the columns containing the electron temperature T_e and the optical depth τ have been added.











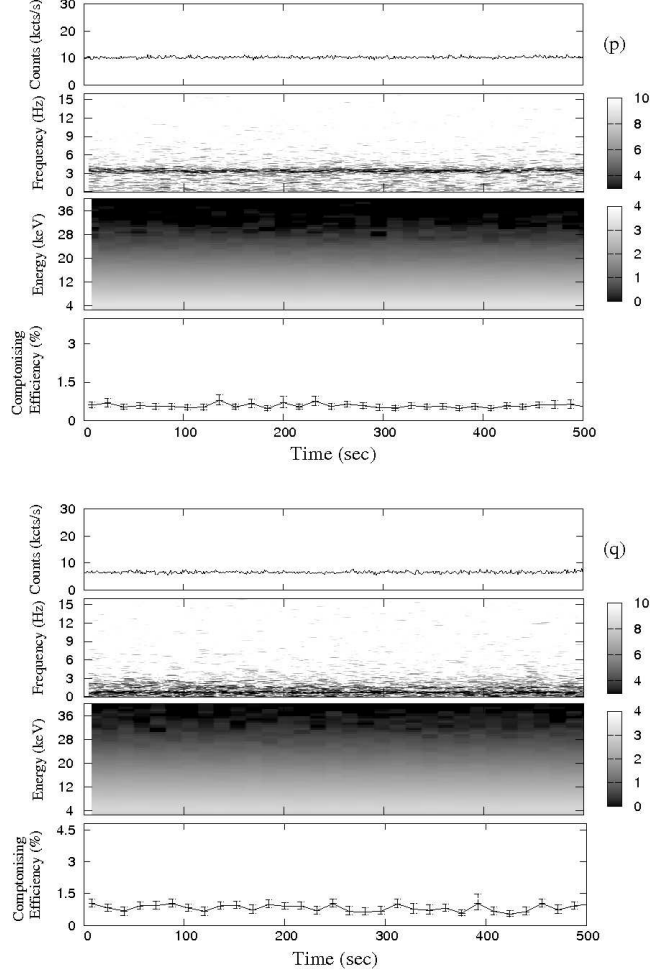


Figure 2: Results of the analysis of (a) I(ϕ), (b) II(δ), (c) III(γ), (d) IV (ω), (e) V(μ), (f) VI(ν), (g) VII(λ), (h) VIII(κ), (i) IX(ρ), (j) X(ξ), (k) XI(β), (l) XII(α), (m) XIII(θ), (n) XIV(χ_2), (o) XV(χ_4), (p) XVI(χ_1), (q) XVII(χ_3), classes are shown. First Panel: Light curve in 2–40 keV range, Middle Panel: Dynamic power density spectra (PDS) of the light curve. Clear evidence of low frequency noise and QPOs are seen. Third panel: Dynamic PCA spectrum showing subtle variations of the spectral characteristics with time. Bottom Panel: Comptonizing Efficiency (CE) in percent, obtained from 16s binned data.

4.1. Class No. I (ϕ)

The Class I data shows a very short time scale variability with the presence of shallow dips in its light curve. The results are shown in Fig. 2a. Dynamic PDS shows no signature of QPOs and the spectrum is mostly soft in nature. The soft photon rate varies at around 330.24 kphotons/s while the Comptonized photon rate varies around 0.16 kphotons/s. The CE is around 0.05%.

4.2. Class No. II (δ)

In Fig. 2b, we show the result of our analysis of the data that belong to the Class II. In this case, there is an absence of QPO in the dynamic PDS and the spectrum is soft, mostly dominated by the blackbody photons. The CE is around 0.06%.

4.3. Class No. III (γ)

The class III data appears to be less variable with a distinct and repeated ‘dip’ like features at a time gap of a few seconds. The result is shown in Fig. 2c. The class is a steady soft state with no QPO visible in the PDS. The CE varies around 0.06%.

4.4. Class No. IV (ω)

The results of the analysis of the data of 1000s in class IV is shown in Fig. 2d. The photon count rate seems to be steady at around 10000 counts/s for most of the time but sometimes for a duration of around 100 sec the photon count is decreased to about 2000 counts/sec. In the whole class, no QPO is observed and whenever the photon count is low, the spectrum appears to become harder. The CE remains low at around 0.07.

4.5. Class No. V (μ)

The result of our analysis for 500s of data of class V is shown in Fig. 2e. In this class, the spectrum, while remaining soft, shows a considerable fluctuation. CE remains low at around 0.05% to 0.15%.

4.6. Class No. VI (ν)

The analysis of 500s of class VI data is shown in Fig. 2f. The fluctuations of the photon count rate and the spectrum are erratic. QPOs are visible. CE varies between 0.04% to $\sim 0.3\%$.

4.7. Class No. VII (λ)

The result of our analysis of 1000 seconds of data of class VII is shown in Fig. 2g. For the first 200 – 600 sec the photon number varies between 10000 and 30000 counts/s. The blackbody photon count of the spectrum is around 300 kphotons/s and Comptonized photon rate is around 0.19 kphotons/s. This class is a mixture of the burst-off and the burst-on states. When the photon count is higher, the spectrum is softer and the object is in the burst-on state and when the photon count rate is lower, the spectrum is harder and object is in the burst-off state. The CE varies between 0.05% to $\sim 0.1\%$. Here too, the physics of varying the Comptonizing region is similar to what is seen in classes VIII-IX below. At the end of the 400s span when the burst-off state starts, a strong spike in both the CE and QPO frequency are observed,

4.8. Class No. VIII (κ)

An analysis of a 500s chunk of the data of class VIII of observation is shown in Fig. 2h. In the class VIII, the photon counts become high ~ 30000 counts/sec and low (~ 10000 counts/sec) aperiodically at an interval of about 50 – 75s. In the low count regions, the spectrum is harder and the object is in the burst-off state. Distinct QPOs are present and at the same time, the Comptonizing efficiency is intermediate, being neither as high as in the class no. XIII-XVI, nor as low as in class I-III. In the fitted spectrum, the Keplerian photon varies between 150 to 450 kphotons/sec and Comptonized photon varies between 0.39 to 0.21 kphotons/sec. The CE becomes high at 0.25%.

4.9. Class No. IX (ρ)

The result of our analysis of the class IX data is shown in Fig. 2i. This class contains a cyclic variation of the hard and soft photons with roughly 75s of periodicity. The blackbody photon count varies between 350 to 420 kphotons/s and Comptonized photons vary around 0.95 to 0.34 kphotons/s. In the harder states CE rises to a maximum of 0.25%.

4.10. Class No. X (ξ)

This class analysis is shown in Fig. 2j. In this class, the photon counts are varying from 2 kcts/s to 8 kcts/s. This is an intermediate class. There is no distinct QPO visible during this observation. For the first 200 sec there is a variation in photon counts. But the spectrum remains soft and the CE is varying less than 0.1%. But during 200s-600s the spectrum becomes

harder and the CE is increased up to 0.3%. Here we see a correlation in the change between the photon counts and the CE variation. During the smaller bumps, the spectrum becomes softer and during the bigger bumps, the spectrum becomes harder.

4.11. Class No. XI (β)

The result of the analysis of 1600s of Class XI data is shown in Fig. 2k. In the first phase of 600 sec, the quasi periodic variation of photon counts takes place with gradually decreasing counts from 10000 counts/s to 30000 counts/s. In this phase, the spectrum is soft and the QPO is seen only when the photon count is low. The CE varies around 0.14%.

In the next 800 sec the spectrum is harder and the distinct variation of QPO frequency (from 12 Hz to 3 Hz) indicates the variation of the shock location. However, in this phase, CE is around 0.27%.

4.12. Class No. XII (α)

Class XII is an intermediate class in which QPO is always observed, the QPO frequency is generally correlated with the count rate (as in XIV-XVII classes discussed below). Since this class displays a long time variation, we analyze the data of 2000s. Fig. 2l shows the result. The CE varies between 0.05% to $\sim 0.6\%$.

4.13. Class No. XIII (θ)

The result of the analysis of a 1000s data of class XIII is shown in Fig. 2m. This class can be divided in two regions depending on the photon count rates. In the soft dip region the photon count rate is lower than 10000 counts/s. In this region, the spectrum is softer and the CE is around 0.17%.

In the other (hard dip) region, say, between 350s and 820s, the photon count is higher and varies from 10000 counts/s to 30000 counts/s. In this region, CE reaches a high value of 0.28%.

4.14. Classes No. XIV (χ_2) & XV (χ_4)

XIV and XV classes have low soft X-ray fluxes with less intense radio emissions. Dynamic PDS shows a distinct QPO at around 3 Hz in class XIV and around 5 Hz in class XV. The X-ray photon is significant up to 40 keV with a flatter power-law slope, which signifies that the source belongs to a harder state. The results are given in Fig. 2n and Fig. 2o. The Comptonizing efficiency in XIV and XV classes is around 0.4 – 0.5%.

4.15. Classes No. XVI (χ_1) & XVII (χ_3)

The classes XVI and XVII correspond to the radio-loud states, whereas the classes XIV and XV are in radio-quiet states (Vadawale et al., 2001). In both the cases, the dynamic PDSs show a strong QPO feature around 4 Hz and 0.8 Hz respectively throughout the particular observation and the spectrum is dominated by the hard power-law. Results are shown in Fig. 2p and Fig. 2q. Around 0.77% of the soft photons are intercepted by the CENBOL in XVI class, whereas it is 0.88% in XVII class.

5. Comptonizing efficiency in different classes: an unifying view

In the above Sections we have analyzed the data of all the seventeen classes. We presented the light curves, the dynamical energy spectra, the power density spectra, and the ratio of the power-law photon rates to the blackbody photon rates obtained from the fit of the original spectra.

To interpret the results, and to facilitate the discussions, it is instructive to keep a paradigm in mind. In Figs. 3(a-c), we present a cartoon diagram which is basically the two component advective flow (TCAF) model of Chakrabarti et al. (1995), suitably modified to include outflows as in Chakrabarti et al. (2000b). In the Figure, the BH represents the black hole, the dark shaded disk is the Keplerian flow and the light shaded disk is the sub-Keplerian flow. The CENBOL, the centrifugal pressure supported boundary Layer of the black hole, and the outflow emanated from it intercept some soft photons from the Keplerian disk and may be cooled down if the Keplerian rate and/or the degree of interception is sufficient.

In the cartoon diagram of Fig. 3a, the CENBOL is not cooled enough and the Comptonization of the soft photon is done both by the CENBOL as well as by the outflow. This configuration typically produces a ‘harder’ state. However, the outflow rate depends on the shock strength (Chakrabarti et al., 1999) and could produce weak jets as in XIV-XV or strong jets as in XVI and XVII (Vadawale et al., 2001). In Fig. 3b, the Comptonization is due to the high accretion rate in the Keplerian disk and the CENBOL collapses. As a result, no significant jet or outflows is expected. This configuration typically produces the softer states. If both the Keplerian and the sub-Keplerian rates are comparable, then the intermediate states would be produced also. In Fig. 3c, we show the situation where the shock strength is intermediate and consequently, the outflow rate is the highest (see, Chakrabarti et al. (1999, 2000b) and references therein). In this case, there is a possibility that

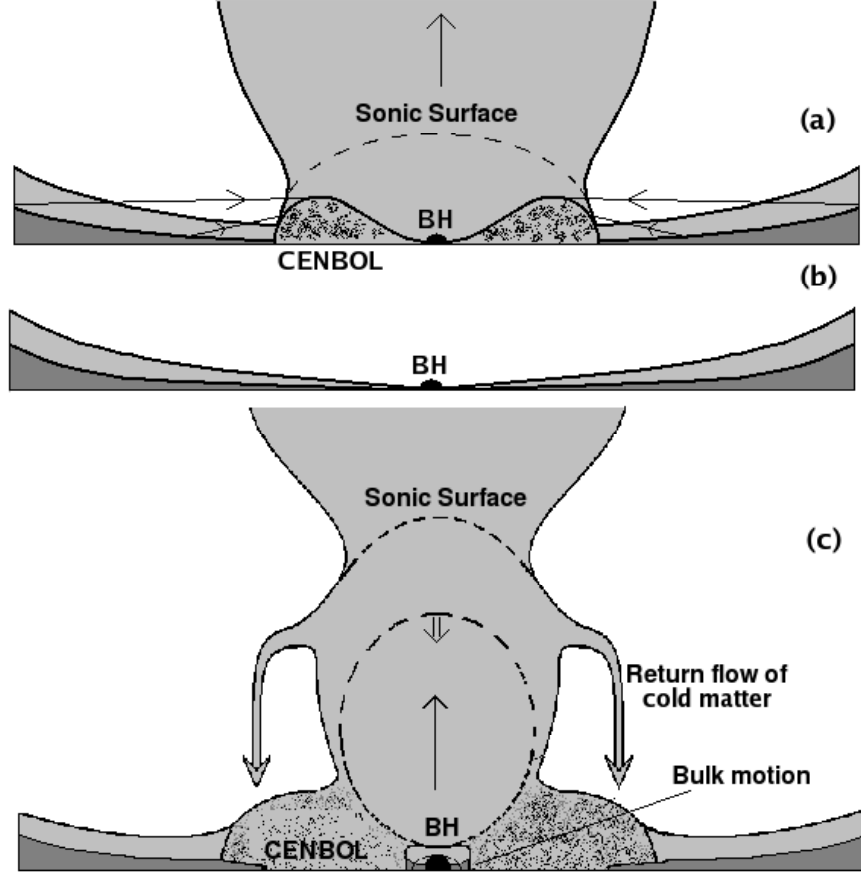


Figure 3: Cartoon diagrams for three major types of variabilities in GRS 1915+105. The classes XIV-XVII belong to the group (a) where the Keplerian rate is low, the CENBOL is large and $\langle CE \rangle$ is high. Jet/outflow rates may be low and continuous. This is the so-called ‘Hard’ group. The softer classes such as I-IV belong to group (b) where the CENBOL is very small and very little Comptonization which could be taking place is due to the sub-Keplerian flows above the Keplerian disk. This is the ‘Soft’ group. The rest of the classes belong to the variation of group (c) or the ‘Intermediate’ group, where, the jet also plays dynamically important role in shaping the spectrum ([Chakrabarti et al., 2000b](#)).

the outflow may be cooled down by Comptonization if the intercepted soft photon flux is high enough and the outflow is temporarily terminated. The flow falls back to the accretion disk, increasing the local accretion rate in a very short time scale (seconds) (Chakrabarti et al., 2000a,b). The possibility of a similar change in local accretion rate was mentioned also by Cabanac et al. (2009). We believe that the variability classes (such as V-XIII) some of which show clear softer (burst-on) and harder (burst-off) states alternately and showed evidences of intermittent jets (Klein-Wolt et al., 2002; Rodriguez et al., 2008) belong to this category (Chakrabarti et al., 2000a).

In TCAF paradigm, results obtained from the analysis are also interpreted. The result obtained for Class No. I(ϕ) and Class No. II(δ) means that a very few black body photons are intercepted by the CENBOL. This corresponds to a situation similar to that in Fig. 3b. In case of Class No. III(γ) the analysis results indicate a low degree of interception of the soft photons with the CENBOL. The four classes I-IV belong to the softer class. The CE is very low, even when the Keplerian rate is high (spectrum is dominated by soft photons). This means that the CENBOL is very small in size and is steady (cooling time scale is much shorter than the infall time scale) and hence the QPOs are also absent. In TCAF paradigm, these cases would correspond to that in Fig. 3b, only the accretion rates vary. From the count rates, it appears that the disk rates are intermediate in classes I and II while it is high in class III. The sub-Keplerian rate is low in class II, but is intermediate in classes I and III. In case of Class No. V(μ) the Keplerian rate may be changing rapidly and the shock is not really formed. This happens when the sub-Keplerian flow has a very low energy and/or angular momentum (Chakrabarti, 1990). In Class No. VII(λ) we can observe an indication of sudden change in the Compton cloud optical depth. In Case of Class No. VIII(κ) burst-off state, low frequency QPOs are indicators of the shock oscillations (Chakrabarti et al., 2000a). As discussed before, in this case, the strength of the shock is intermediate and produces strong outflows (Chakrabarti et al., 2000a). In case of burst-on state of the same class the CENBOL would be cooled down. Some matter returns back from the wind on the CENBOL. When it is totally drained, the burst-off state is resurfaced with a lower CE (less than 0.1%). In case of Class No. XI(ρ) the harder states (low count regions), the CENBOL is prominent and the Keplerian component is farther away. Thus the QPO is prominent. Interception of black body photons increases with CENBOL size and CE rises to a maximum of 0.25%. As the Keplerian disk moves towards the black hole, a gradual softening of the spectrum occurs since the CENBOL

becomes smaller in size while still retaining its identity. At the peaks of the light curve, the CENBOL, which is also the base of the jet is cooled down due to the increased optical depth. In case of Class No. XI (β) the outflow is taking an active role in intercepting the soft-photons. We suspect that sudden rise in magnetic activity occurs in this case which collapses the CENBOL due to increased magnetic tension in the hotter plasma (Nandi et al., 2001b). In case of Class No. XII (α) the spectrum shows that the Keplerian rate is not changing much, but the sub-Keplerian flow fluctuates, perhaps due to failed attempt to produce sporadic jets. This case may also require parameters outside the scope of TCAF to understand fully. For Class No. XIII (θ) The QPO is also present. Here, the CE, which is linked to the geometry of the Comptonizing region, is anti-correlated with the QPO frequency. In TCAF paradigm, QPO this is correlated with shock location, i.e., the CENBOL size. In the third panel, where the dynamic spectrum is drawn, we note that between the soft dip and the hard dip, the low energy photon intensity is not changing much, while the intensity of spectrum at higher energies is higher. This indicates that the sub-Keplerian rate is high in the hard dip state. Here too the presence of a strong magnetic field may be required to understand this class fully. In Class No. XIV (χ_2) and XV (χ_4) the CENBOL is big in size and the Keplerian disk is farther out and/or with a very low rate. In case of Class No. XVI (χ_1) and XVII (χ_3) according to TCAF paradigm, the CENBOL (Fig. 3a) oscillates to produce the observed QPOs (Chakrabarti et al., 1997, 2000a). The Keplerian rate is low and is unable to cool the CENBOL and the jet combined. Whether the outflow rate would be high or low would depend on the shock strength (Chakrabarti et al., 1999).

In the literature, to our knowledge, there has been no discussion on the sequence in which the class transitions should take place. Also, there is no discussion on which physical properties of the flow the variability classes depend. In the above, we analyzed several aspects of the variability classes which may be understood physically from the two component advective disk paradigm. Since CE behaves differently in various classes, it may play an important role in distinguishing various classes. This CE is directly related to the optical depth of the Compton cloud, since the optical depth determines the fraction of the injected soft photon intercepted by the Comptonizing region.

Though CE varies in a given class, it is instructive to compute the average CE in a given class (averaged over a period characterizing the class). The average is computed as follows: $\langle CE \rangle = \Sigma(CE_h Dt_h + CE_s Dt_s) / \Sigma(Dt_h + Dt_s)$,

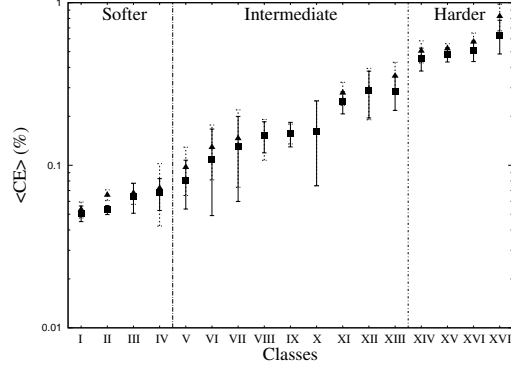


Figure 4: Variation of the average Comptonizing efficiency ($\langle CE \rangle$) for different variability classes of GRS 1915+105. The error-bars were calculated from the excursion of CE in a given class. Filled squares and triangles represent $\langle CE \rangle$ for two sets of variability classes. Softer classes have smaller $\langle CE \rangle$ and harder classes have higher $\langle CE \rangle$.

where, the subscripts h and s under CE denote its value when the spectrum is harder (for a residence time of Dt_h) and softer (for a residence time of Dt_s) respectively. $Dt_h + Dt_s$ denotes the full cycle time of a given class. We denote this as $\langle CE \rangle$. In Fig. 4, we present the variation of $\log(\langle CE \rangle)$ in various classes. We placed ‘error bars’ also in all the average values which are at 90% confidence level. These ‘error-bars’ are actually the excursion of $\langle CE \rangle$ in that class, and not actually the error-bars in the usual sense. We arranged the classes in ascending order of $\langle CE \rangle$. This gives rise to a sequence of the variability class shown in the X-axis. In classes XI and XIII, we did not average CE over both hard and soft regions, since it is believed that the soft regions are produced due to sudden disappearance of the Compton cloud (Nandi et al., 2001a). Thus, while placing them in the plot, we considered the average over the burst-off (harder) state only. To show that the sequence drawn is unique, we plotted the average values of CE of two sets of data (Table 1). The average of the first set is drawn with a dark square sign and the average of the second set is drawn with a dark triangle sign. The individual error bars are drawn with solid and dashed lines respectively. In both the sets, the sequence is identical. Based on the nature of the variations of CE, we divided these classes into three groups corresponding to three types of accretion shown in Figs. 3(a-c). Classes I to IV belong to the ‘softer’ states and classes XIV-XVII belong to the ‘harder’ states. The rest of the classes belong to the ‘intermediate’ states.

Once we sequence the classes based on $\langle CE \rangle$, one could ask if the

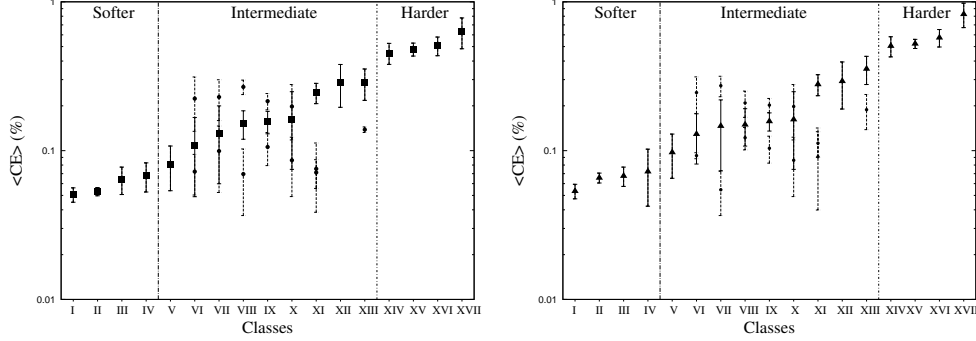


Figure 5: Variation of average Comptonizing efficiency ($\langle CE \rangle$) for different variability classes of GRS 1915+105. In the left panel, we show the results for the data set plotted with filled squares in Fig. 4, and the right panel, we show the results of the data plotted with filled triangles in Fig. 4. The averages in hard and soft chunks are placed separately with filled circles. In class XI averages of three chunks (burst on, pre-spike and post-spike) are plotted with filled circle, filled box and filled circle respectively. The overall sequence is found to remain the same in both sets of data. We placed classes XI and XIII according to $\langle CE \rangle$ in the hard (pre-spike) region since the softer regions are believed to be produced due to totally different physical processes.

sequence means anything, physically and observationally. Physically, increasing average $\langle CE \rangle$ corresponds of increasing optical depth of the Comptonizing region and its excursion signifies how the optical depth varies in short timescales, i.e., accretion rate in the low-angular momentum component (Fig. 3). Observationally, only a handful class transitions have been caught ‘red-handed’. About them we shall discuss later below.

In Figs. 5(a-b), we plotted the results of these two sets of analysis separately. We separate the averages over CE in the burst-off and burst-on states (as dark filled circles) when they are present as well as the global average over CE in a given class by filled squares (except classes XI and XIII where the physics is different and it is meaningless to talk about the overall average; and hence only average over the harder region is plotted.).

In Chakrabarti et al. (2004, 2005), it was mentioned that although many RXTE observations were made of GRS 1915+105, only in a few cases, direct transitions were observed. In particular, using Indian X-ray Astronomy Experiment (IXAE) it was shown that the direct transitions of $\kappa \rightarrow \rho$ (VIII \rightarrow IX), $\chi \rightarrow \rho$ (XIV \rightarrow IX), $\chi \rightarrow \theta$ (XIV \rightarrow XIII) and $\rho \rightarrow \alpha$ (IX \rightarrow XII) do take place in a matter of hours. In Naik et al. (2002b), IXAE data was used to argue that ρ class variability could have changed to χ class via α

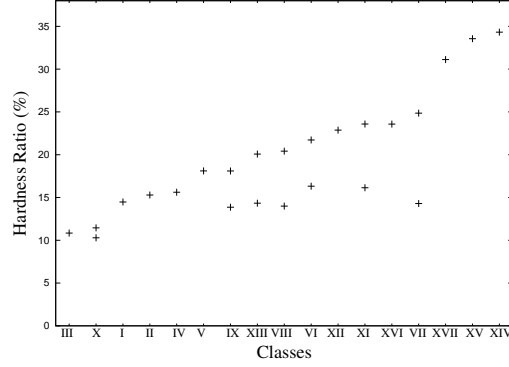


Figure 6: Variation of the hardness ratio for different variability classes of GRS 1915+105. The hardness ratio is the ratio between (10 - 40 keV) and (2 - 10 keV) photon counts in %. A sequence of variability classes in X-axis is obtained by placing the hardness ratios in ascending order. For intermediate states the hardness ratio of the harder portions is used for the sequencing of the classes. This sequence is totally different from that presented in Fig. 5 and is not connected to any observed transition.

class (i.e., $IX \rightarrow XII \rightarrow XIV$). In [Nandi et al. \(2001b\)](#), it was shown that the θ class (Class XIII) is anomalous and the observed soft-dip is perhaps due to the disappearance of the CENBOL by magnetic rubber band effect (this is the magnetized TCAF or MTCAF model). Accepting the class XIII to be anomalous, we find from Fig. 4 that the observed transitions reported in [Chakrabarti et al. \(2004, 2005\)](#); [Naik et al. \(2002b\)](#) are ‘naturally’ explained. For instance, $\chi \rightarrow \rho$ (θ and β being anomalous and intermediate α has been reported by [Naik et al. \(2002b\)\), \$\rho \rightarrow \alpha\$ \(\$\beta\$ being anomalous\) and \$\kappa \rightarrow \rho\$, are expected from our analysis. We believe that if we carry out spectrophotometry of GRS 1915+105 continuously \(\[Chakrabarti et al., 2008\]\(#\)\), then we may be able to catch the transition from one type to another more often and check if the sequences we mentioned here are sufficiently robust or need further refinement.](#)

In Fig. 6, we plotted the variation of the conventional hardness ratio for all the classes of GRS 1915+105 for the sake of comparison of CE. Here, the hardness ratio is the ratio (in %) between the photon rates in (10 - 40 keV) and in (2 - 10 keV) range. The classes are arranged in the ascending order of hardness ratios. In case of intermediate classes we have taken the hardness ratio of the harder portions. This sequence obtained from this Figure does not seem to have any special significance in that it does not support the observed class transitions reported in [Chakrabarti et al. \(2004, 2005\)](#).

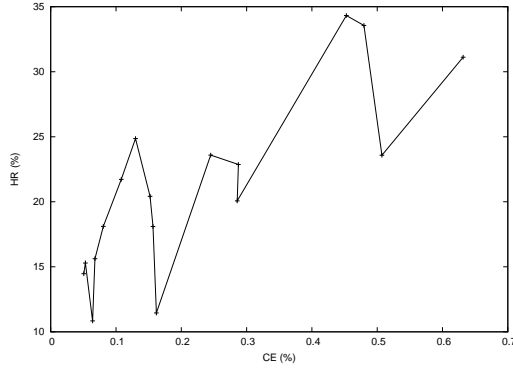


Figure 7: Variation of HR(%) vs CE(%) of GRS 1915+105. The definition of HR is same as given in Fig. 6. CE is plotted in ascending order but the variation of HR do not follow the same sequence along with the variation of CE.

In Fig. 7, we plotted the variation of the variation of conventional HR for all classes along with the CE for GRS 1915+105. This Figure shows that the variation of HR do not follow one to one correspondence with the variation of CE.

The conventional hardness ratio is generic as it is not based on any radiative processes. It is independent of even the black hole mass and accretion rates. That is the main reason why the CE defined by us may be considered to be more physical.

6. Conclusions

In this paper, we have analyzed all known types of variability classes of the enigmatic black hole GRS1915+105 and computed the dynamical nature of the energy and the power density spectra. We did not characterize these classes by conventional means, such as the hardness ratios defined in certain energy range since such a characterization does not provide us with any insight about the physical picture. Furthermore, characterization using conventional hardness ratio can be done on a case by case basis, and cannot be valid for the black holes of all masses. Because of this we concentrated on the ratio of the photon fluxes in the power-law and black body components as seen in the disk frame. This is a quantity similar to the conventional hardness ratio, but the energy ranges automatically vary from class to class as obtained by minimizing χ^2 . We asked ourselves whether we can distinguish one class from another from physical point of view independent of

what the nature of the Compton cloud is. We computed the mean $\langle CE \rangle$ Comptonizing efficiency and put them in an ascending order. This sequence remains the same in two independent sets of data we studied. So $\langle CE \rangle$ may be thought of characterizing a class. Based on the values of $\langle CE \rangle$, it is observed that the classes belong to three states: Classes I-IV belong to the softer states, Classes V-XIII belong to the intermediate states, and Classes XIV-XVII belong to the harder state.

Surprisingly, the handful of class transitions in GRS 1915+105 which have been caught ‘red-handed’ appear to take place between the nearest neighbors of this sequence. It is hoped that the transitions observed in future may also take place between two nearest neighboring classes unless the neighboring class itself is anomalous (such as, θ , β and α which appear to require enhanced magnetic activities). If so, then it would imply that the average optical depth of the Compton cloud (which is decided by the specific angular momentum and the accretion rate of the low-angular momentum halo, according to [Chakrabarti et al. \(1995\)](#) model) holds an important key to decide a variability class. Neither the accretion rate of the Keplerian disk nor the accretion rate of the low-angular momentum matter alone individually can be considered to be the deciding factor.

In the two component model of [Chakrabarti et al. \(1995\)](#), the CENBOL and the associated outflow play the role of the Compton cloud. In this model, a change in CE can be achieved in several ways: (i) A change in the shock location (achieved by changing primarily the specific angular momentum) change the size of the CENBOL and thus the degree of interception of soft photons, and/or, (ii) by changing the accretion rate of the sub-Keplerian component, which changes the optical depth and scatter a different number of soft photons to produce the power-law photons. However, the survival of the Compton cloud depends on the accretion rate in the Keplerian component. If the rate is higher, the Compton cloud collapses. Thus, CE is the result of non-linear relationships among the flow parameters. In [Chakrabarti et al. \(1995, 1997\)](#) the spectral state variation was shown to be due to these effects. In our present situation, we find that the classes with harder states have more CE. However, since shifting the shock location or raising the sub-Keplerian rate does not involve viscous effects, changes in softer to harder states or vice versa can be achieved in minutes or even seconds. The time scales of such effects through a Keplerian flow could take days. Thus, we believe that not only we identify the most important parameter which distinguishes from one class to the other, we also believe that it is understandable within the

framework of the TCAF model.

While we obtain a hint that the $\langle CE \rangle$ is important in deciding the class transition sequence, for a given class, the degree of excursion of CE in a given variability type must depend on another parameter, such as the outflow rate. In the TCAF picture, a simple estimate (Chakrabarti et al., 1999) suggests that the shock strength decides the outflow rate and therefore the time taken by the base of the outflow to reach $\tau \sim 1$ for a Compton scattering to take place (Chakrabarti et al., 2000a). Thus the outflow rate also decides the time-scale for which a class will stay in a harder or softer states, which in turn, decides the degree of excursion of CE in a given class. For a very strong shock, the outflow rate is very weak, as is evidenced by a weak radio flux even for ‘radio-loud’ classes. For intermediate shock strength the outflow rate is higher, and it is easier to have $\tau = 1$ in a short time scale (Chakrabarti et al., 2000a). The fractional change in CE can also become high. In classes XIII-XVII, we not only find CE to be very high, the excursion of CE is very small as well. The aspect of classification in terms of the outflow rate is being looked into. The analysis is in progress and will be reported elsewhere.

It is to be noted that GRS 1915+105 has been observed, though intermittently, for over 17 years now and we have analyzed only few tens of data sets, each lasting for ~ 2000 s. Thus it is likely that more exhaustive data sets or future observations may force us to re-look at the sequence that we prescribe here. One limitation of our work is that we do not include the effects of the hardening factor of the spectra in separating the power-law and the black body photons. With the present understanding of the anomalous classes such as β and θ , it is not yet clear why sometimes these classes are skipped while transiting from one class to another, other than to speculate that these classes require a new parameter, such as strong magnetic fields, which may be due to magnetic activity of the companion star. With an improvement in understanding a further refinement of our sequence may not be ruled out.

7. Acknowledgment

PSP acknowledges SNBNCBS-PDRA Fellowship.

References

Belloni, T., Klein-Wolt, M. & Mendez, M. et al., A model-independent analysis of the variability of GRS 1915+105, *A&A*, 355, 271-290, 2000.

- Cabanac, C., Fender, R. P. & Dunn, R. J. H. et al., On the variation of black hole accretion disc radii as a function of state and accretion rate, MNRAS, 396, 1415-1440, 2009.
- Castro-Tirado, A. J., Brandt, S. & Lund, S., GRS 1915+105, IAU Circ, 5590, 2-2, 1992.
- Castro-Tirado, A. J., Alberto, J. & Brandt, S., et al., Discovery and observations by watch of the X-ray transient GRS 1915+105, ApJS, 92, 469-472, 1994.
- Chakrabarti, S. K., *Theory of Transonic Astrophysical Flows*, World Scientific Co., 1990.
- Chakrabarti, S. K. & Titarchuk, L. G., Spectral Properties of Accretion Disks around Galactic and Extragalactic Black Holes, ApJ, 455, 623-639, 1995.
- Chakrabarti, S. K., Spectral Properties of Accretion Disks around Black Holes. II. Sub-Keplerian Flows with and without Shocks, ApJ, 484, 313-322, 1997.
- Chakrabarti, S. K., Estimation and effects of the mass outflow from shock compressed flow around compact objects, A&A, 351, 185-191, 1999.
- Chakrabarti, S. K. & Manickam, S. G., Correlation among Quasi-Periodic Oscillation Frequencies and Quiescent-State Duration in Black Hole Candidate GRS 1915+105, ApJ, 531, 41-44, 2000a.
- Chakrabarti, S. K. & Nandi, A., Fundamental States of Accretion/Jet Configuration and the Black Hole Candidate GRS1915+105, IJP, 75B(1), 1-4, 2000b.
- Chakrabarti, S. K., Nandi, A., Manickam, S. G. & Mandal, S. et al., Spectral Signature of Mass Loss from (and Mass Gain by) an Accretion Disk around a Black Hole, A&A, 579, 21-24, 2002.
- Chakrabarti, S. K., Nandi, A., Choudhury, A. & Chatterjee, U., Evidence of Class Transitions in GRS 1915+105 from Indian X-Ray Astronomy Experiment Data, ApJ, 607, 406-409, 2004.

- Chakrabarti, S. K., Nandi, A. & Chatterjee, A. K et al., Class transitions and two component accretion flow in GRS 1915+105, *A&A*, 431, 825-830, 2005.
- Chakrabarti, S. K. & Majumder, A. S., *Observational Evidence for Black Holes in the Universe, (Ed.) S.K. Chakrabarti*, 409, (AIP: NY), 2008.
- Dunn, R. J. H., Fender, R. P. & Krding, E. G. et al., A global spectral study of black hole X-ray binaries, *MNRAS*, 403, 61-82, 2010.
- Greiner, J., Morgan, E. H. & Remillard, R. A., Rossi X-Ray Timing Explorer Observations of GRS 1915+105, *ApJ*, 473, 107-110, 1996.
- Hannikainen, D. C., Rodriguez, J. & Vilhu, O. et al., Characterizing a new class of variability in GRS 1915+105 with simultaneous INTEGRAL/RXTE observations, *A&A*, 435, 995-1004, 2005.
- Harlaftis, E. T. & Greiner, J., The rotational broadening and the mass of the donor star of GRS 1915+105, *A&A*, 414, 13-16, 2004.
- Klein-Wolt, M., Fender, R. P. & Pooley, G. G. et al., Hard X-ray states and radio emission in GRS 1915+105, *MNRAS*, 331, 745-764, 2002.
- Makishima, K., Maejima, Y. & Mitsuda, K. et al., Simultaneous X-ray and optical observations of GX 339-4 in an X-ray high state, *ApJ*, 308, 635-643, 1986.
- Migliari, S. & Belloni, T., Evidence for local mass accretion rate variations in the disc of GRS 1915+105, *A&A*, 404, 283-289, 2003.
- Mikles, V. J., Varniere, P. & Eikenberry, S. S. et al., Quasi-Periodic Oscillation Frequency-Color Radius Connection in GRS 1915+105: A Possible Turnover Supporting Accretion-Ejection Instability Predictions, *ApJ*, 694, 132-135, 2009.
- Mirabel, I. F. & Rodriguez, L. F., A superluminal source in the Galaxy, *Nat*, 371, 46-48, 1994.
- Morgan, E. H., Remillard, R. A. & Greiner, J., RXTE Observations of QPOs in the Black Hole Candidate GRS 1915+105, *ApJ*, 482, 993-1010, 1997.

- Morrison, R. & McCammon, D., Interstellar photoelectric absorption cross sections, 0.03-10 keV, *ApJ*, 270, 119-122, 1983.
- Muno M. P., Morgan, E. H. & Remillard, R. A., Quasi-periodic Oscillations and Spectral States in GRS 1915+105, *ApJ*, 527, 321-340, 1999.
- Naik, S. & Rao, A. R., Disk-jet connection in GRS 1915+105: X-ray soft dips as cause of radio flares, *A&A*, 362, 691-696, 2000.
- Naik, S., Rao, A. R., & Chakrabarti, S. K., Fast Transition between High-soft and Low-soft States in GRS 1915 + 105: Evidence for a Critically Viscous Accretion Flow, *JApA*, 23, 213-234, 2002a.
- Naik, S., Agrawal, P.C., Rao, A.R. & Paul, B., X-ray properties of the microquasar GRS 1915+105 during a variability class transition, *MNRAS*, 330, 487-496, 2002b.
- Nandi, A., Manickam, S. G. & Chakrabarti, S. K., Classification of Light curves of the Black Hole Candidate GRS1915+105, *IJP*, 74B, 331-339, 2000.
- Nandi, A., Manickam, S. G. & Chakrabarti, S. K., On the source of quasi-periodic oscillations of the black hole candidate GRS 1915+105: some new observations and their interpretation, *MNRAS*, 324, 267-272, 2001a.
- Nandi, A., Chakrabarti, S.K., Vadawale, S.V. & Rao, A.R., Ejection of the inner accretion disk in GRS 1915+105: The magnetic rubber-band effect, *A&A*, 380, 245-250, 2001b.
- Nayakshin, S., Rappaport, S. & Melia, F., Time-dependent Disk Models for the Microquasar GRS 1915+105, *ApJ*, 535, 798-814, 2000.
- Neilsen, J. & Lee, J. C., Accretion disk winds as the jet suppression mechanism in the microquasar GRS 1915+105, *Nat*, 458, 481-484, 2009.
- Neilsen, J., Remillard, R. A. & Lee, J. C., The Physics of the “Heartbeat” State of GRS 1915+105, *ApJ*, 737, 69-89, 2011.
- Pal, P. S., Nandi, A. & Chakrabarti, S. K., Dynamical Nano Quasar GRS 1915+105, *AIPC*, 1053, 209-213, 2008.

- Rao, A. R., Yadav, J. S. & B. Paul, Rapid State Transitions in the Galactic Black Hole Candidate Source GRS 1915+105, *ApJ*, 544, 443-452, 2000a.
- Rao, A. R., Naik, S., Vadawale, S. V. & Chakrabarti, S.K., X-ray spectral components in the hard state of GRS 1915+105: origin of the 0.5 - 10 Hz QPO, *A&A*, 360, 25-29, 2000b.
- Rodriguez, J., Durouchoux, P. & Mirabel, I. F et al., Energy dependence of a low frequency QPO in GRS 1915+105, *A&A*, 386, 271-279, 2002.
- Rodriguez, J., Shaw, S. E. & Hannikainen, D. C. et al., 2 Years of INTEGRAL Monitoring of GRS 1915+105. II. X-Ray Spectro-Temporal Analysis, *ApJ*, 675, 1449-1458, 2008.
- Shimura, T. & Takahara, F., On the spectral hardening factor of the X-ray emission from accretion disks in black hole candidates , *ApJ*, 445, 780-788, 1995.
- Sobczak, G. J., McClintock, J. E., & Remillard, R. A. et al., RXTE Spectral Observations of the 1996-1997 Outburst of the Microquasar GRO J1655-40, *APJ*, 520, 776-787, 1999.
- Steiner, J. F., Reis, R. C. & McClintock, J. E. et al., The spin of the black hole microquasar XTE J1550-564 via the continuum-fitting and Fe-line methods, *MNRAS*, 416, 941-958, 2011.
- Sunyaev, R. I. & Titarchuk, L.G., Comptonization of X-rays in plasma clouds - Typical radiation spectra, *A&A*, 86, 121-138, 1980.
- Sunyaev, R. A. & Titarchuk, L. G., Comptonization of low-frequency radiation in accretion disks Angular distribution and polarization of hard radiation, *A&A*, 143, 374-388, 1985.
- Titarchuk, L. G., Generalized Comptonization models and application to the recent high-energy observations, *ApJ*, 434, 570-586, 1994.
- Ueda, Y., Yamaoka, K. & Remillard, R., GRS 1915+105 in “Soft State”: Nature of Accretion Disk Wind and Origin of X-ray Emission, *ApJ*, 695, 888-899, 2009.

- Vadawale, S. V., Rao, A. R., Nandi, A. & Chakrabarti, S. K., Observational evidence for mass ejection during soft X-ray dips in GRS 1915+105, *A&A*, 370, 17-21, 2001.
- Vadawale, S. V., Rao, A. R. & Naik, S. et al., On the Origin of the Various Types of Radio Emission in GRS 1915+105, *ApJ*, 597, 1023-1035, 2003.
- Vignarca, F., Migliari, S. & Belloni, T. et al., Tracing the power-law component in the energy spectrum of black hole candidates as a function of the QPO frequency, *A&A*, 397, 729-738, 2003.
- Yadav, J. S., Rao, A. R. & Agrawal, P. C., et al., Different Types of X-Ray Bursts from GRS 1915+105 and Their Origin, *ApJ*, 517, 935-950, 1999.